



Optimization of hybrid friction stir welding of PMMA: 3D-printed parts and conventional sheets welding efficiency in single- and two-axis welding traces

Markos Petousis¹ · Nikolaos Mountakis¹ · Nectarios Vidakis¹

Received: 12 March 2023 / Accepted: 22 May 2023 / Published online: 3 June 2023
© The Author(s) 2023

Abstract

Herein, the feasibility of joining with the friction stir welding (FSW) process 3D-printed parts made of poly(methyl methacrylate) (PMMA) with extruded PMMA sheets is investigated. A full factorial design method is followed, with two control parameters, i.e., tool rotational and travel speed, and three levels each. The hybrid joints produced were subjected to tensile and flexural loading and the corresponding properties were optimized with statistical modeling tools. Regression analysis provided prediction models for the five output metrics. The temperature was monitored throughout the experimental process. Samples were inspected with optical and scanning electron microscopy and their morphological characteristics were correlated with the joining conditions. The optimized FSW parameters were used for joining PMMA 3D-printed parts with sheets with two-axis joining seams. The produced hybrid joints were more than sufficient in their mechanical properties. The highest welding efficiency achieved in the tensile tests was 1.36, by the sample welded with 900 rpm and 6 mm/min. The sample welded with the same conditions achieved also the highest welding efficiency in the flexural tests (0.98). The findings presented proven the efficiency of the hybrid PMMA joints studied and have direct industrial applications for efficient component production.

Keywords Poly(methyl methacrylate) · Material extrusion · Hybrid additive manufacturing · Optimization · Friction stir welding · Fused filament fabrication

Nomenclature

3DP	3D printing	F-sB	Flexural strength
ABS	Acrylonitrile butadiene styrene	FFD	Full factorial design
AM	Additive manufacturing	FFF	Fused filament fabrication
ANN	Artificial neural networks	FSW	Friction stir welding
ANOVA	Analysis of variances	HAZ	Heat-affected zone
AS	Advancing side	HAM	Hybrid additive manufacturing
BT	Bed temperature	HDPE	High-density polyethylene
CNC	Computer numeric control	MAPE	Mean absolute percentage error
DOE	Design of experiment	MCU	Machine control unit
DSC	Differential scanning calorimetry	MEP	Main effect plot
F-E	Flexural modulus of elasticity	MEX	Material extrusion
		NT	Nozzle temperature
		NZ	Nugget zone
		PA	Polyamide
		PLA	Polylactic acid
		PET-G	Polyethylene terephthalate glycol
		PMMA	Poly(methyl methacrylate)
		PP	Polypropylene
		PS	Print speed
		RDA	Raster deposition angle
		RS	Rotational speed

✉ Nectarios Vidakis
vidakis@hmu.gr

Markos Petousis
markospetousis@hmu.gr

Nikolaos Mountakis
mountakis@hmu.gr

¹ Hellenic Mediterranean University, 71410 Heraklion, Greece

RTS	Retreating side
RPM	Revolutions per minute
SEM	Scanning electron microscopy
SV	Side view
SZ	Stirring zone
T-E	Tensile modulus of elasticity
T-sB	Tensile strength
T _g	Glass transition temperature
TGA	Thermogravimetric analysis
TMAZ	Thermomechanically affected zone
TPU	Thermoplastic polyurethane
TS	Travel speed
TV	Top view
WE	Weld efficiency
WT	Welding temperature

1 Introduction

AM is increasing its popularity in industrial fields such as the manufacturing of functional parts, product development, and tooling [1]. This is owed to its advantages, such as the ability to produce parts without geometrical constraints, lightweight, and facilitating customization [2, 3]. Among the disadvantages of the AM process is that it is slow for large part production [4], especially considering that for simple shape parts, such as sheets, traditional methods are optimized many years now. To overcome the restrictions of AM and further expand its applicability, hybrid additive manufacturing (HAM) has been introduced, which combines AM with traditional manufacturing processes. For example, to improve the dimensional accuracy and the surface quality of polymeric 3D-printed parts, made with PET-G [5], ABS [6], PLA nanocomposites with carbon black [7], or carbon nanotubes [8] as the additive, AM processes have been integrated with CO₂ laser cutting processes. To increase the build size capacity of polymeric parts, made with PA6 [9], PMMA [10], PLA [11], high-density polyethylene (HDPE)/carbon black (CB) composites [12], and ABS [13], AM has been integrated with the FSW joining process. Still, research on the joining of polymeric materials with the FSW is rather limited, especially for 3D-printed parts, in which the 3D-printing structure is an additional challenge [9]. The differences in the performance of 3D-printed and bulk polymeric materials in FSW have been pointed out in the literature [14].

FSW is a process developed for joining mainly aluminum parts in applications in which traditional processes were not possible to be applied [15]. Due to its characteristics, it is popular in industrial fields, such as the aerospace industry and the automotive sector, among others [16, 17]. Research in aluminum is very wide in the literature [15, 18, 19]. The process parameter and their effect on the performance of

the seam is a popular subject [15, 18, 20–25], while different aluminum grades have been investigated [26–31]. Aspects, such as the mechanical properties of the welds, their wear and corrosion performance, and the effect of thermal treatment, have been investigated [32, 33]. Aluminum tailor-welded blanks have also been produced with the FSW process [34]. Other alloys, such as magnesium, have been investigated for their performance under dynamic loading [35]. Often dissimilar (hybrid) joints are studied for the performance of joints between two different materials, such as aluminum and polymer materials [36] or aluminum with steel [37].

PMMA is a synthetic polymer. It is optically clear and therefore it is utilized as a replacement for inorganic glass [38]. Due to its characteristics, it is popular in various glass and non-glass related applications in fields, such as membranes [39, 40], solar applications [38], electrical [41], energy storage [42–46], cranioplasty [47–51], dentistry [52, 53], and generally in biomedical applications [54]. Although many polymers have been extensively researched in additive manufacturing (AM), including polypropylene (PP) [55], polyamide 12 (PA12) [56], acrylonitrile–butadiene–styrene (ABS) [57], and polyethylene terephthalate glycol (PETG) [58], among others, research is still limited on the PMMA polymer [59]. The primary areas of interest include biomedical behavior and applications in vat photopolymerization 3D printing [60, 61], such as bone scaffold research [62]. The mechanical properties of 3D-printed parts made with the PMMA polymer have been investigated [63–65]. Also, the energy consumption during the 3D printing of PMMA parts with the MEX process has been reported in an attempt to optimize the energy demands and the mechanical performance of the parts [66]. The feasibility of joining PMMA sheets [67, 68] or PMMA with aluminum sheets [69] with FSW has been investigated. The performance of joints produced with the FSW process for 3D-printed PMMA parts with the MEX process has been reported, as mentioned above [10]. Modeling tools have been applied for the analysis and optimization of the experimental findings regarding the performance of 3D-printed parts, making the process a common approach in the literature [70, 71]. The full factorial design approach has been employed for the analysis and optimization of the performance of welds produced on 3D-printed PLA parts, joined with the FSW process [11]. Therefore, to be consistent with the existing literature, a similar method was applied in the current study.

Herein, the feasibility of hybrid joints welded with the FSW process and combining PMMA 3D-printed parts and sheets is investigated. For the first time in the literature, according to the authors' best knowledge, a hybrid weld with friction stir welding is attempted, with injection molded and 3D-printed PMMA parts, fabricated with the MEX process. At the same time, for the first time, a two-dimensional seam

is attempted, with a complex shape, combining all the different types of plane shapes. The performance of the weld and the phenomena that occurred during the process are presented and compared with corresponding linear welds to evaluate the effect of the two-dimensional seam paths in the process. Such joints have merit for industrial applications, in which PMMA sheets, which are not possible or it is not cost-efficient to be produced with AM processes, can be joined with 3D-printed PMMA components with complex geometry. Such components in specific applications cannot be integrated into the sheet with a different approach than welding.

The feasibility of such hybrid joints is studied herein employing a full factorial design method, with two control parameters and three levels each, i.e., rotational speed and travel speed. Since the performance of the FSW process in joining 3D-printed PMMA parts has been reported [10], the tool that produced the best results was used herein. The welded hybrid samples were tested for their mechanical performance in tensile and flexural tests and their morphological characteristics were evaluated with optical microscopy and SEM. Throughout the FSW process, the temperature was recorded to check the state of the materials during the joining process. Results were processed with statistical modeling tools and regression analysis provided prediction models for the five response indicators studied. The optimization results were further exploited in the investigation of the feasibility of two-axis hybrid weld seams, which is the second field this study innovates. More specifically, 3D-printed PMMA parts were welded with bulk PMMA sheets, with seams of various shapes, covering any possible formation (single- and two-axis paths). Samples were prepared with various fitting shapes between them, assembled, and welded with the FSW process applied along the two parts' contact (two-axis) edge. The produced seam was evaluated with microscopy for defects and voids. It was found that it is possible to produce hybrid joints with 3D-printed and bulk PMMA parts employing the FSW process, with joined parts having in several cases welding efficiency higher than one, even in a two-axis welding scenario. Such results are valuable information for the industry and can be directly exploited in corresponding applications.

2 Materials and methods

2.1 Experimental procedure

Figure 1a shows the raw materials drying in the laboratory oven (40 °C for 4 h). PMMA pellets were procured from JULIER (Fujian, China). Transparent 4-mm PMMA bulk sheets were also procured from the local market. The thermal properties of the procured PMMA were determined

with TGA and DSC. TGA measurements were derived on a Perkin Elmer Diamond TG/TDA (Waltham, MA, USA), with the following heating scenario 40–550 °C, step 10 °C/min, nitrogen purge gas. DSC measurements were derived on a Perkin Elmer Diamond DSC (Waltham, MA, USA), with the following heating scenario 25–220–25 °C, step: 15 °C/min. The thermal property investigation aimed to prove that the temperatures used in the filament extrusion process, the MEX 3D-printing process, and the FSW process that followed do not affect the thermal stability of the PMMA polymer. Figure 1b shows the filament extrusion process on a 3devo precision (Utrecht, The Netherlands) single screw extruder, which produces compatible with the MEX 3D-printing process (1.75 mm diameter). The filament was further dried before the 3D-printing process (Fig. 1c, 40 °C for 4 h).

Figure 1d shows the MEX 3D-printing process on an Intamsys Funmat HT (Shanghai, China) machine. PMMA samples were 3D printed (Fig. 1e) with the settings derived from the literature (Fig. 2) [66]. Their dimensions are also shown in Fig. 2a, and they were made to fit the fixture (Fig. 1f) manufactured for the FSW of 3D-printed samples. Analytically the functionality of the fixture is explained in previous works in the literature [10, 13]. Figure 1g shows the FSW process for the hybrid seam (3D-printed and bulk PMMA sheet fitted as shown in Fig. 2b). FSW was performed on Haas (Oxnard, CA, USA) TM-1P three-axis milling CNC machine. The required G-code program was compiled directly in the machine's MCU. The FSW settings are depicted in Fig. 2 and they were derived from the literature [10]. The optimum FSW settings derived from the study on the performance of seams when joining PMMA 3D-printing parts were employed herein [10]. In this direction, the welding tool that achieved the highest performance in joining PMMA 3D-printed parts with the FSW process was used herein and is shown in Fig. 2c. The manufacturing process of this welding tool is presented analytically in a previous study [10].

During the FSW process, to validate the state of the material, the developed temperature was recorded with a thermal imaging camera (Flir One Pro, Teledyne FLIR LLC, China). The completed seam produced with the FSW process in this hybrid scenario is shown in Fig. 1h. After the completion of the FSW process, the welded sample was cut into specimens for the mechanical tests that followed (Fig. 1i). Twelve specimens were cut from the welded sample, with batches of four being welded with the same TS. The welded hybrid samples after the cut process are shown in Fig. 1j. These samples were tested for their mechanical performance in tensile (Fig. 1k) and flexural tests (Fig. 1l).

To assess the effect of the FSW process on the Vickers microhardness of the material, measurements were taken (400-Vickers, Innova Test Europe BV, Maastricht, The

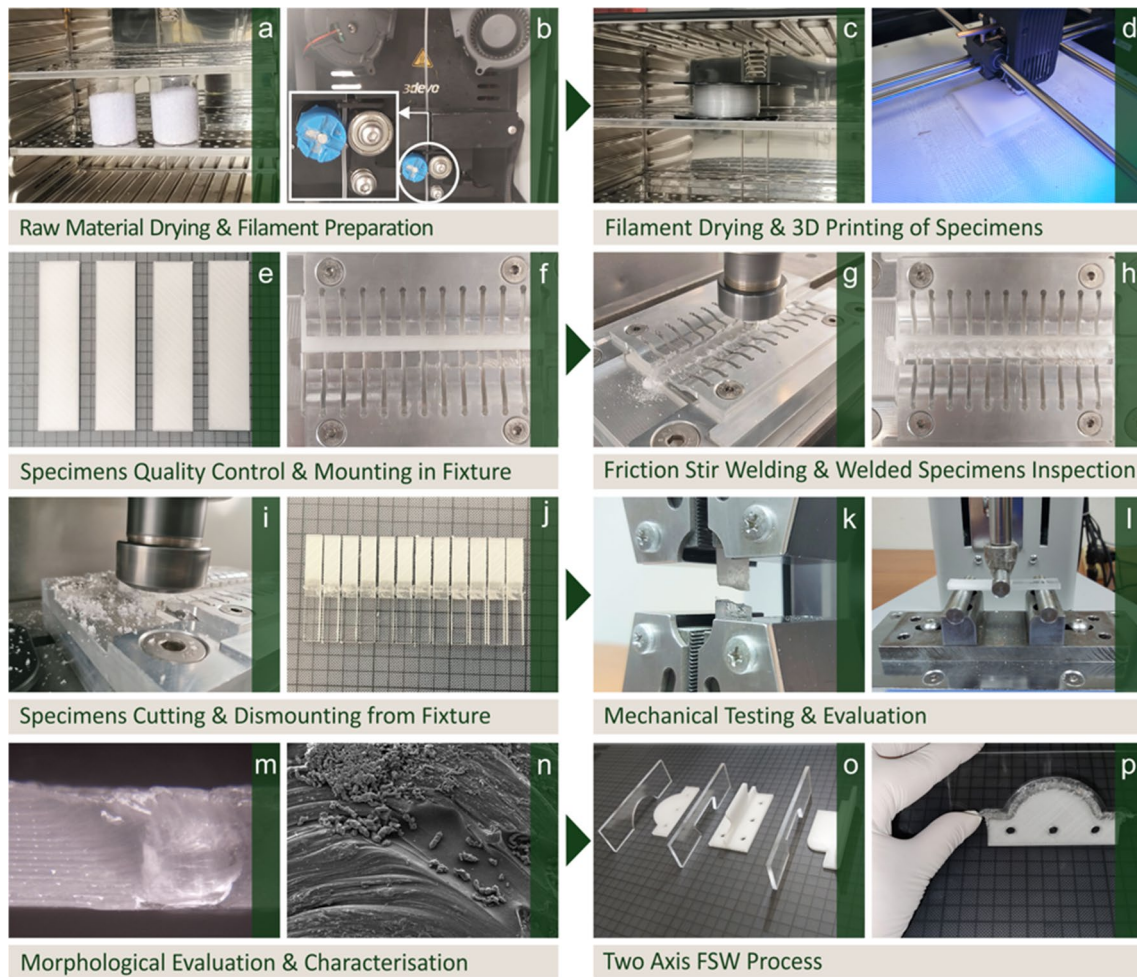
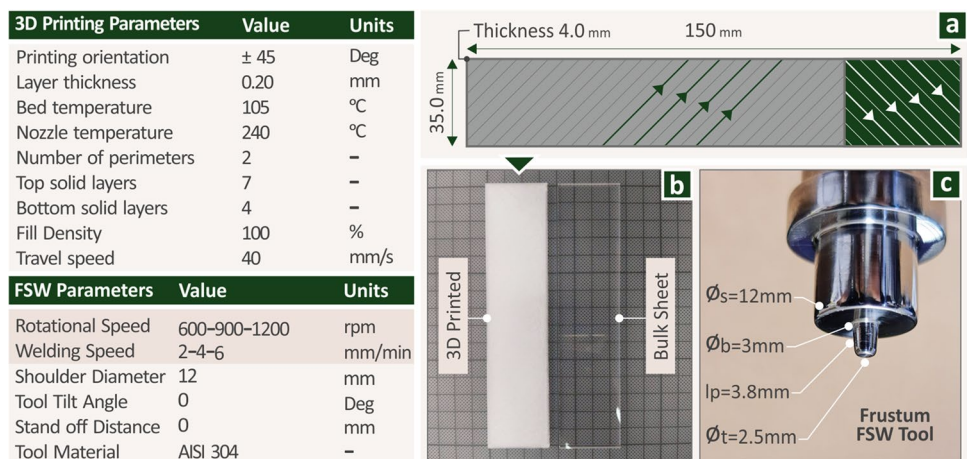


Fig. 1 **a** Drying of the raw materials, **b** extrusion of the filament, **c** drying of the filament, **d** workpieces 3D printing, **e** 3D-printed PMMA sheets, **f** fixture setup, **g** specimens joining with the FSW process, **h** the seam produced, **i** tensile test specimens cutting process, **j** the hybrid tensile specimens (PMMA 3D-printed and bulk

sheet samples joined with FSW), **k** tensile testing, **l** flexural testing, **m** optical microscopy, **n** morphological characterization with SEM, **o** 3D-printed and bulk material PMMA parts for two-axis joining with FSW, and **p** two-axis seam

Fig. 2 Parameters used in the MEX 3D printing and the FSW process: **a** dimensions of the 3D-printed samples, the 3D printing structure is also presented; **b** 3D-printed and bulk PMMA samples prepared for the FSW process, and **c** the FSW weld tool used



Netherlands) on the side surface of the hybrid samples (ASTM E384 standard) on the 3D-printed side, the bulk sheet side, and the weld zone. Measurements were taken on various positions along the height of the sample (from bottom to top) in all three regions. Afterward, the mechanical tests were carried out in an Imada MX2 apparatus (IL, USA). The testing conditions were an elongation speed of 10 mm/min, 23 °C, and 50% humidity. The flexural tests were three-point bending tests with a 52-mm support span.

After the completion of the mechanical tests, the morphological characteristics at the weld region of the specimens were examined with an optical microscope (Kern OKO 1, Kern & Sohn, Albstadt, Germany), a stereoscope (KERN OZR5, Kern & Sohn, Albstadt, Germany) (Fig. 1m), and SEM (JSM-IT700HR field emission SEM device, 20 kV acceleration voltage, gold-coated specimens, Jeol, Tokyo, Japan) (Fig. 1n). The weld morphology and the fracture mechanism were evaluated in these observations.

2.2 Design of experiments

The full factorial design method was followed herein. The control parameters were the rotational speed and the travel speed with three levels each herein. As mentioned above, the control parameters and their levels were selected according to the literature for the welding with the FSW method of 3D-printed PMMA parts built with the MEX process [10]. The control parameter levels are presented in Fig. 2. As mentioned, the weld tool, which is critical for the performance of the weld in the FSW process [72], was the one that achieved optimum mechanical response in the aforementioned research. Five were the output metrics that were evaluated and optimized with this approach, i.e., WT, T-E, T-sB, F-E, and F-sB. Regression analysis was followed to derive suitable prediction models for these five metrics as functions of the control parameters.

2.3 Two-axis FSW

To further evaluate the feasibility of the hybrid joint studied herein and provide proof of its applicability in real industrial components, test cases were carried out using the control parameter values that achieved the best results in the linear seam hybrid joint. To test all the possible part-fitting scenarios, two-axis seams were conducted, having single- and two-axis welding paths (linear, curvilinear, acute, right, and obtuse angles, and combinations of those). These types of joints with various seam shapes were initially designed with a Computer-Aided Design (CAD) software tool. The parts and their fitting edge were designed to be able to be assembled and fit, covering the aforementioned test scenarios. Again, one part of the joint was from the PMMA bulk sheet and the other was 3D printed, with the parameters

mentioned above. When the two parts of the hybrid joint were manufactured (3D printed and cut properly according to the design for the PMMA sheet), they were assembled and fitted (Fig. 1o). Then they were welded with the FSW process with the most suitable control parameter values, as mentioned (Fig. 1p). The produced seam was inspected with microscopy for defects. In this more complex welding scenario, the feasibility of producing hybrid PMMA joints with the FSW process was proven.

3 Results

3.1 FSW of the hybrid PMMA joint

Figure 3a shows a screenshot from the FSW process. Material's flacking during the process is shown in the figure. As mentioned, the linear seam is divided into three equal-length regions. In each region, different FSW conditions are applied. The RS is kept constant throughout the seam. At the end of the first region, the TS is increased, then is kept constant until the end of the second region, and then is further increased at the third region, until the completion of the seam. With this procedure, three batches of four samples each of welded specimens with the same conditions are produced. At the beginning of the seam, the weld tool enters the seam from the side; it is not submerged in the seam. At the point of entry to the seam, the weld tool stops its linear displacement while it is still rotating for some time. This ensures that both the weld tool and the specimens have reached an adequate temperature for the FSW process and the seam is implemented under the same conditions. Welding debris is scattered on the top surface of the hybrid joint during the process. These come from superficial strands or parts that are not welded and fend off the welding zone (Fig. 3b). Throughout the FSW process, the temperature at the weld zone is monitored and recorded as mentioned. The maximum recorded temperature in each one of the three regions in which different TS was applied as shown in Fig. 3c. As shown, the temperature increases with the increase of the TS; still, the recorded temperature values indicate that the required solid state of the materials during the FSW process was maintained throughout the process.

After the completion of the FSW process, the two specimens are welded with a linear seam, with the conditions explained above. Each one of the three regions in which the weld is performed with different TS produces for four specimens for the mechanical tests. Therefore, each welded joint is able to produce twelve specimens in total, in batches of four same samples (regarding the FSW conditions, the dimensions are the same in all the samples) for the mechanical tests. Before the removal of the welded sample, a tool

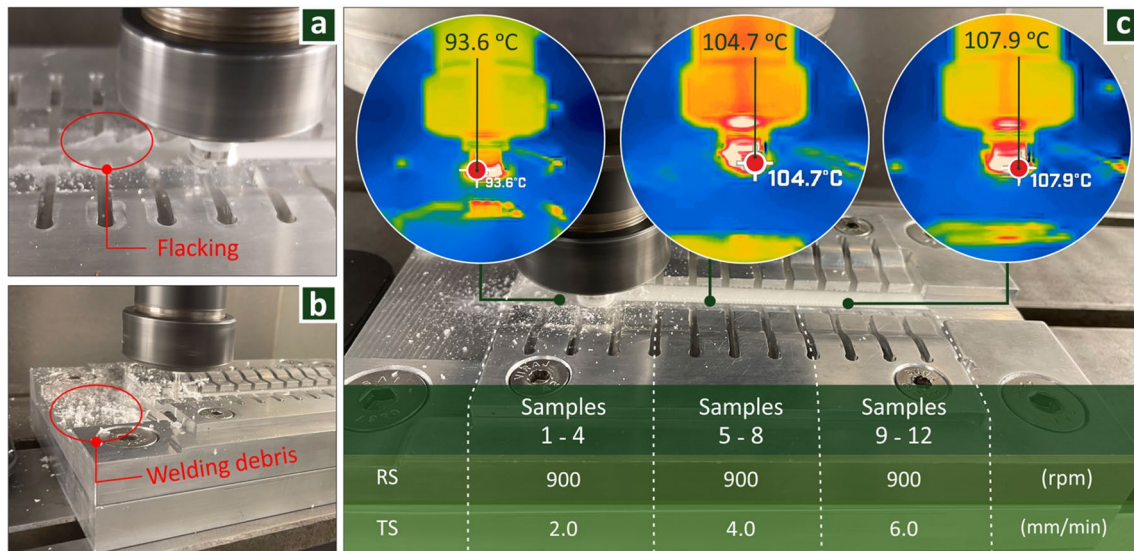


Fig. 3 **a** FSW process in which the flaking of the specimens is shown, **b** welding debris produced during the FSW process, and **c** the temperatures developed along the seam during the FSW process

change is performed, and a suitable cutting tool is selected in the spindle of the CNC milling machine for the cutting of the workpiece into the twelve specimens for the mechanical tests. The fixture used is designed in a way that enables this process to be performed automatically directly in the CNC machine right after the FSW process. In this way, twelve specimens ready for the mechanical tests are acquired at the end of the CNC machine procedure with one fixture of the fixture device and the workpiece in the CNC machine.

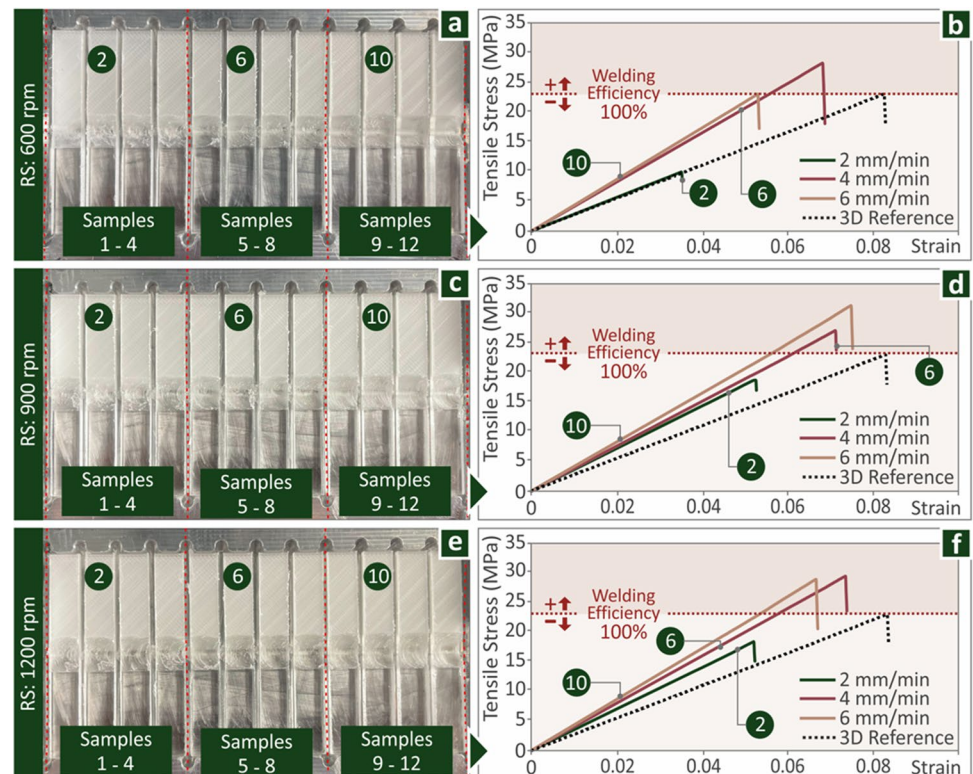
3.2 Mechanical tests

The hybrid samples welded with the FSW process with various conditions (control parameter values) are shown in Fig. 4a (600 rpm RS), c (900 rpm RS), and e (1200 rpm RS). Next to each picture, stress vs. strain graphs are presented for specimens welded with the corresponding RS and all the TS values studied. The graph from one randomly selected sample out of the four welded with the same TS and the specific RS is shown (Fig. 4b, 600 rpm RS; d, 900 rpm RS, and f, 1200 rpm RS). The stress vs. strain curve of a solid, not welded 3D-printed sample is also shown in each graph, as the control sample. In all RS values, the specimen welded with 4 mm/min TS achieved welding efficiency higher than 1. The weld efficiency is the ratio between the strength of the welded sample and the strength of the corresponding solid (not welded) one. Values higher than 1 indicate that the strength of the welded sample is increased compared to the not welding one, which is the desirable outcome of a welding process. At the same time, the samples welded with 2 mm/min TS showed decreased strength in all RS values. Samples

welded with 6 mm/min TS had weld efficiency higher than 1 in the cases of 900 and 1200 rpm RS, while at 600 rpm RS, the samples has weld efficiency of approximately 1, which is also a well-acceptable result. In all cases, specimens failed in the weld nugget zone, and only at 2 mm/min TS specimens failed at the thermomechanically affected zone (TMZ), as shown below in the morphological analysis of the samples. In the supplementary material for the work, the corresponding mechanical test results in the flexural tests are presented. In the flexural tests, overall, the increase in the RS increased the performance of the weld. Again, the samples welded with 2 mm/min TS showed decreased strength in all RS values, and overall samples marginally reached weld efficiency of 1.

Vickers microhardness measurements were taken on the 3D-printed side, the weld zone, and the bulk PMMA material side of the hybrid joints, on various positions along the height of the sample (from bottom to the top) and presented in Fig. 5. As shown, the bulk PMMA microhardness measurements are the highest ones. The measurements are decreased in the weld zone and further decreased in the 3D-printed side of the hybrid joint. The samples welded with 600 rpm and 900 rpm RS show a constant increase in the Vickers microhardness measurements from the 3D-printed side to the weld zone and the bulk side, with the increase being steeper on the 900 rpm RS sample. The sample welded with 1200 rpm RS shows a non-constant increase in the Vickers microhardness measurements in the three zones (3D printed, welded, and bulk material), as the samples welded with the other two RS values show.

Fig. 4 Samples welded with various RS. On the right side, the corresponding stress vs. strain graphs for the samples welded with the specific RS and the different TS applied is presented. The welding efficiency is also indicated, compared to the 3D-printed PMMA part **a**, **b** 600 rpm, **c**, **d** 900 rpm, and **e**, **f** 1200 rpm



3.3 Thermal properties and temperature during the FSW process

TGA showed that the PMMA grade used in the study starts to degrade at 310 °C (Fig. 6a). DSC showed that the melting point of the PMMA grade used in the study is at 194 °C (Fig. 6c). These results verified that the temperatures used in the extrusion process for the filament production and the MEX 3D-printing process do not affect the thermal stability of the material or cause any degradation. Figure 6b shows the maximum temperature values in all the FSW cases implemented in the study. As shown, all temperatures are approximately between 50 and 150 °C (< 194 °C). So, the temperature values recorded show that the PMMA polymer was in a solid state during the FSW process, which is the required status for the material during the FSW process. In the supplementary material, the temperature measurements are presented and organized per the different cases studied.

3.4 Morphological characterization

The morphology of the side surface of the welded hybrid joints was initially inspected with stereoscopy and optical microscopy (Fig. 7). The expected formation of the weld zone is clearly observed, with the SZ, the TMAZ, and the HAZ having a rather similar in shape formation along the advancing side (AS) (3D-printed sample) and the retreating

sample (RTS) (bulk material) [73]. The 3D-printing structure on the AS is visible (Fig. 7a) and so is the bulk material structure on the RTS (Fig. 7c). The entire weld zone is presented in Fig. 7b. The pile-up of the material on the AS (Fig. 7d) and the surface downside on the RTS (Fig. 7e) can also be observed, while a bottom pit was formed as shown in Fig. 7d and e. In Fig. 7f and g defects of the weld, such as cavitations and unwelded areas, are presented. In this case, such defects were found on the AS probably due to the 3D-printing structure, which has internal pores and cavities [74]. During the FSW process of polymeric 3D-printed parts, the porosity is reduced in the weld zone and a surface downside is expected [9], which was not very intense herein. Still, this is common in bulk materials as well [75]. It was observed in the RTS and it affects the strength of the parts since the cross-section area of the sample is reduced [9].

Optical stereoscope and optical microscope images of the weld zone of the hybrid joint for three samples welded with different FSW settings are presented in Fig. 8. The first-row image presents the side surface of the hybrid joint, the second-row presents images from the top side of the weld zone, and the third row presents images of the three samples from the top side after they fail in the mechanical tests. In these images, the profile of the fracture surface from the top is shown to evaluate differences in the deformation of the samples before their failure and the area in which failure occurred in the experiments. In the side surface images

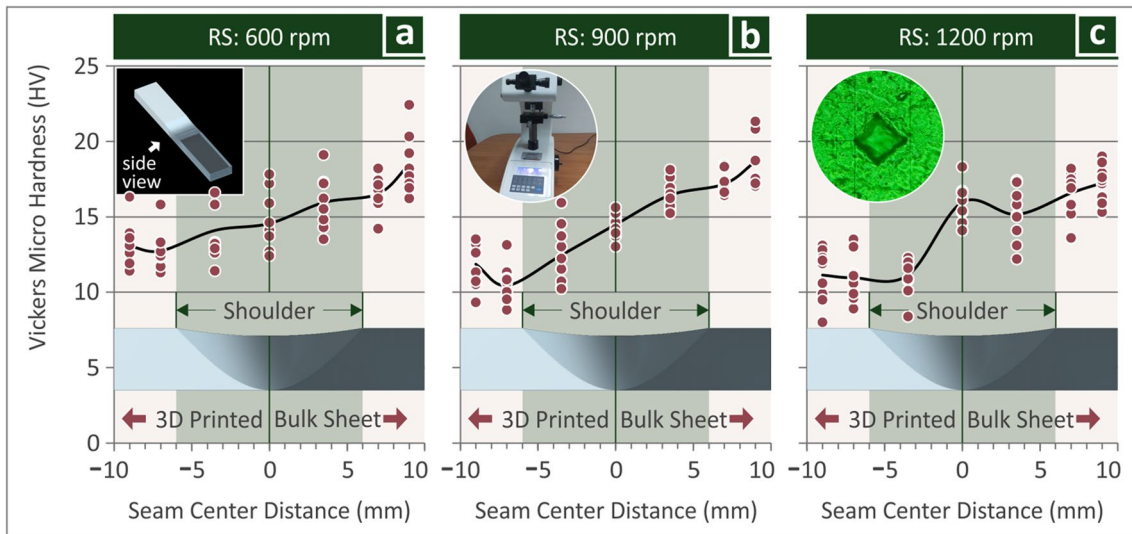


Fig. 5 Vickers microhardness measurements on the side surface of the welded hybrid samples. Measurements were taken on the 3D-printed side, the weld zone, and the bulk PMMA material side, on

various positions along the height of the sample (from bottom to the top): **a** 600 rpm RS, **b** 900 rpm RS, and **c** 1200 rpm RS

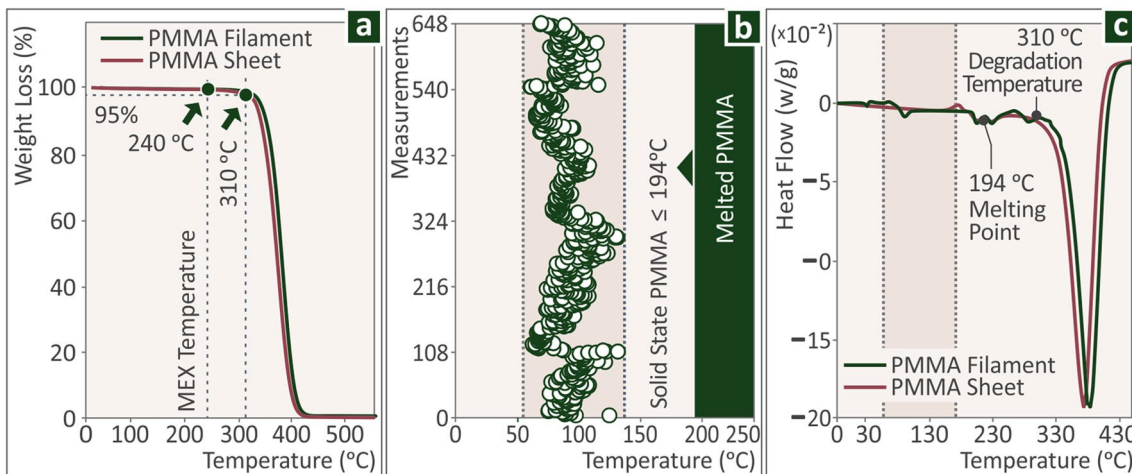


Fig. 6 **a** Weight loss vs. temperature (TGA), **b** the maximum temperature recorded in all repetitions of the FSW process, and **c** heat flow vs. temperature (DSC)

(Fig. 8a, d, and g), the different FSW zones are outlined. The nugget zone (NZ) (or stirring zone, SZ) is cylindrical in all cases and extends to the bottom of the samples. The width of the NZ differs in the samples, with the sample welded with lower RS and TS values having a wider diameter NZ. The other two samples are approximately the same in width.

The TMAZ zones also differ. The sample welded with lower RS and TS values (600 rpm and 2 mm/min, Fig. 8a) shows a wider TMAZ. In this sample, the TMAZ shape also differs between the AS and the RTS, with the TMAZ on the RTS side being wider. As the RS and TS values increase (900 rpm and 4 mm/min, Fig. 8d), the TMAZ is

narrower and almost symmetrical in shape between the AS and the RTS side. Further increase in the RS and TS values (1200 rpm and 6 mm/min, Fig. 8g) slightly increases the width of the TMAZ. The size of the TMAZ in this case is almost the same in the AS and the RTS but the shape differs. The top surface images of the weld zone show that the sample welded with higher FSW settings (1200 rpm and 6 mm/min, Fig. 8h) has a more smooth surface. The sample welded with 900 rpm and 4 mm/min (Fig. 8e) has the more rough surface among the three samples. The sample welded with lower RS and TS values (600 rpm and 2 mm/min (Fig. 8b) also has a rough surface

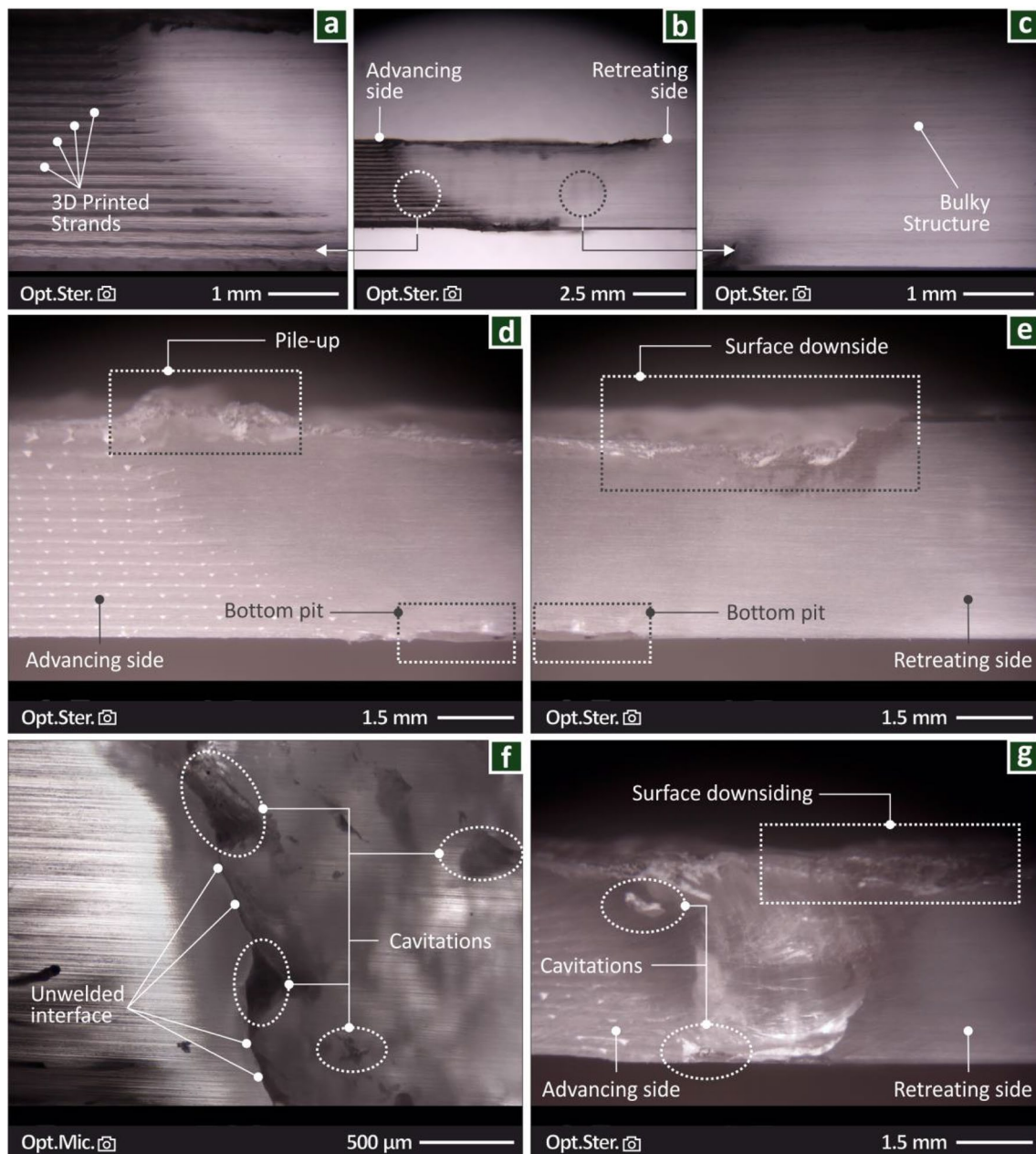


Fig. 7 Optical stereoscope images from the side surface of the **a** 3D-printed sample, **b** weld zone, **c** bulk PMMA side, **d** material pile-up on the advancing side (3D printed), **e** surface downside on the retreating side (bulk material), **f** optical microscopy image showing

unwelded interfaces and cavitation on the side surface, and **g** stereoscopic image showing cavitations on the advancing side and surface downsizing on the retreating side

but is less rough than the sample shown in Fig. 8e. In all cases the typical circular welding marks are visible in the images.

The images from the top, after the failure of the samples in the tensile tests, show differences in the failure of the samples (Fig. 8c, f, and i). In the sample welded with lower RS and TS values (600 rpm and 2 mm/min, Fig. 8c), a brittle fracture can be observed with almost no deformation visible in the image. The failure occurred in the TMAZ from

the AS. As the RS and TS values increase (900 rpm and 4 mm/min, Fig. 8f), some deformation occurred in the sample before its failure, still a rather brittle fracture mechanism is shown. In the sample welded with higher FSW settings (1200 rpm and 6 mm/min, Fig. 8i), a more ductile failure is presented with deformation visible in the fracture area. In the samples shown in Fig. 8f and I, failure occurred in the NZ and not in the TMAZ zone as in the sample welded with lower RS and TS values.

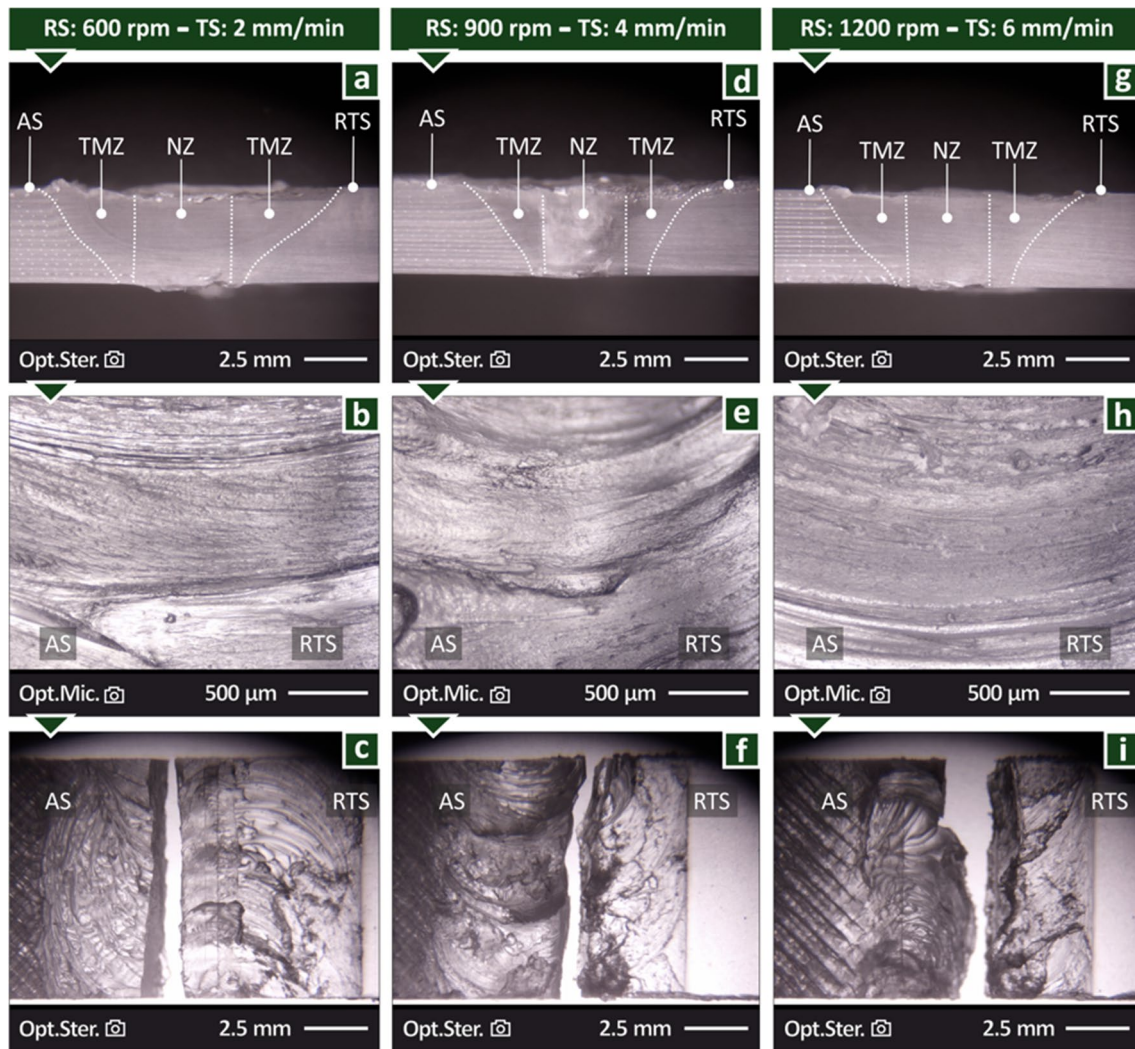


Fig. 8 Optical stereoscope images from the side surface of the weld zone for samples welded with **a** RS 600 rpm, TS 2 mm/min; **d** RS 900 rpm, TS 4 mm/min; **g** RS 1200 rpm, TS 6 mm/min. Optical microscope images from the top side of the weld zone for samples welded with **b** RS 600 rpm, TS 2 mm/min; **e** RS 900 rpm, TS 4 mm/min; **h** RS 1200 rpm, TS 6 mm/min. Optical stereoscope images after the failure of the parts in the tensile tests, depicting the fracture profile of the weld zone from the top for samples welded with **c** RS 600 rpm, TS 2 mm/min; **f** RS 900 rpm, TS 4 mm/min; and **i** RS 1200 rpm, TS 6 mm/min

Figure 9 presents SEM images of the top surface of two different samples, one welded with the lowest FSW conditions studied (600 rpm RS and 2 mm/min TS, Fig. 9a, b, and c) and one with the highest FSW conditions studied (1200 rpm RS and 6 mm/min TS, Fig. 9d, e, and f). Images were taken at three different magnification levels of $\times 30$, $\times 300$, and $\times 2000$, at the AS on the samples. At the $\times 30$ magnification images (Fig. 9a, and d), the strands of the 3D-printing structure are visible along with their deformation on the area in which the weld zone starts. In this area, the welding marks are visible and marked in the figures. At the $\times 300$ magnification images (Fig. 9b, and e), friction micro-debris are shown. In the sample welded with higher RS and TS values (Fig. 9e), the surface is more smooth than

the samples welded with lower RS and TS values (Fig. 9b). At the $\times 2000$ magnification images (Fig. 9c, and f), micro-cavitations and trenches are visible, which could not be identified in lower magnification images.

SEM images from the fracture surface of the samples, after the completion of the mechanical tests, are presented in Fig. 10, at $\times 25$ magnification. The two same samples' fracture surface is depicted from the tensile and the flexural test. In all specimens, micro-cracks are observed in the fracture surface. The flexural test specimens (Fig. 10c and d) show a more brittle fracture surface than the corresponding tensile test samples (Fig. 10a and b). In the flexural test samples, the one welded with lower RS and TS values (Fig. 10c) slightly deformed before its failure, but still, a brittle failure

the samples welded with lower RS and TS values (Fig. 9b). At the $\times 2000$ magnification images (Fig. 9c, and f), micro-cavitations and trenches are visible, which could not be identified in lower magnification images.

SEM images from the fracture surface of the samples, after the completion of the mechanical tests, are presented in Fig. 10, at $\times 25$ magnification. The two same samples' fracture surface is depicted from the tensile and the flexural test. In all specimens, micro-cracks are observed in the fracture surface. The flexural test specimens (Fig. 10c and d) show a more brittle fracture surface than the corresponding tensile test samples (Fig. 10a and b). In the flexural test samples, the one welded with lower RS and TS values (Fig. 10c) slightly deformed before its failure, but still, a brittle failure

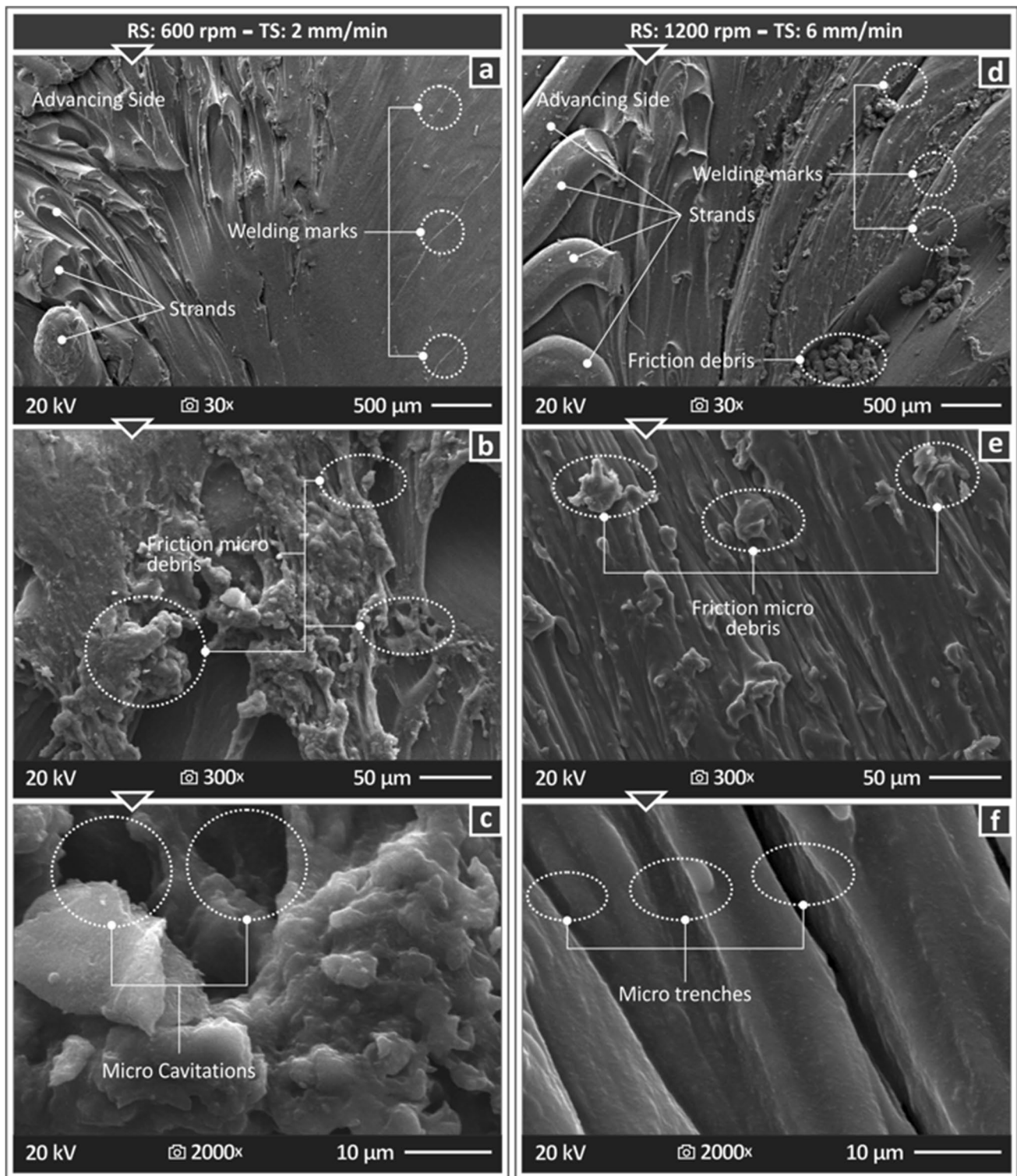


Fig. 9 SEM images taken on the top of the samples in the weld zone at a magnification of $\times 30$, $\times 300$, and $\times 2000$, respectively, for samples welded with **a–c** RS 600 rpm, TS 2 mm/min; **d–f** RS 1200 rpm, TS 6 mm/min

occurred. In the tensile test samples (Fig. 10a and b), the sample welded with lower RS and TS values (Fig. 10a) had a more brittle behavior, with lower deformation visible

compared to the sample welded with higher RS and TS values (Fig. 10b). This agrees with the findings presented above in the stereoscope images (Fig. 8) and the mechanical

test results. Samples welded with lower RS values showed a more brittle behavior than samples welded with higher RS values. Still, the unwelded 3D-printed part used as a reference showed the least brittle behavior among the samples tested. The micro-cracks shown in the SEM images for the fracture surface are typical in polymeric materials with brittle behavior [76, 77].

3.5 Experimental findings with the FFD

The full factorial design (FFD) is presented in Table 1. The control parameter values in each run are depicted along with the average values and deviation for the five response metrics of the study, i.e., WT, T-sB, F-sB, T-E, and F-E. Three replicas were tested in each run and the experimental results for each repetition of the experiments in each run are available in the supplementary material of the work.

Figures 11 and 12 present the MEP and the interaction plots for the five metrics studied. The increase in the RS and the TS increases the WT. Higher TS values increase both the T-sB and the T-E. The increase of the RS increases the stiffness of the samples (T-E), while the median value of RS achieved the highest T-sB value among the three RS levels. A different effect is shown in the flexural test properties, with the increase of RS increasing both the F-sB and

the F-E. Higher TS values also increased both the F-sB and the F-E. Only the median value of TS decreased the F-E. Regarding the interaction plots, in all metrics, synergistic relations were found.

3.6 Regression analysis

The quadratic regression model (QRM) for each response is calculated:

$$Y_k = \alpha_{i,k} + \sum_{i=1}^n b_{i,k}x_i + \sum_{i=1}^n c_{i,k}x_i^2 + \sum_i \sum_j d_{ij,k}x_i x_j + e_k \quad (1)$$

where k represents the response output (e.g., welding temperature, tensile strength, flexural strength, tensile modulus of elasticity, and flexural modulus of elasticity), a is the constant value, b is the coefficients of the linear terms, c is the coefficients of the square terms, d is the coefficients of the two-way interaction terms, e is the error, and x_i the seven ($n = 2$) control parameters, i.e., the rotational speed (RS), travel speed (TS).

Regression tables were formed (Tables 2, 3, 4, 5, and 6) for the five metrics studied and corresponding prediction models as functions of the control parameters (Eqs. (2)–(6)) [78]. In all metrics, the p -values were almost 0 and the f -values were much higher than four (4). The lowest calculated regression value was 77.04 % among the five metrics. Such results

Fig. 10 SEM images taken after the completion of the mechanical tests on the fracture surface of the samples at a magnification of $\times 25$ tensile tests: **a** RS 600 rpm, TS 2 mm/min; **b** RS 1200 rpm, TS 6 mm/min, flexural tests; **c** RS 600 rpm, TS 2 mm/min, and **d** RS 1200 rpm, TS 6 mm/min

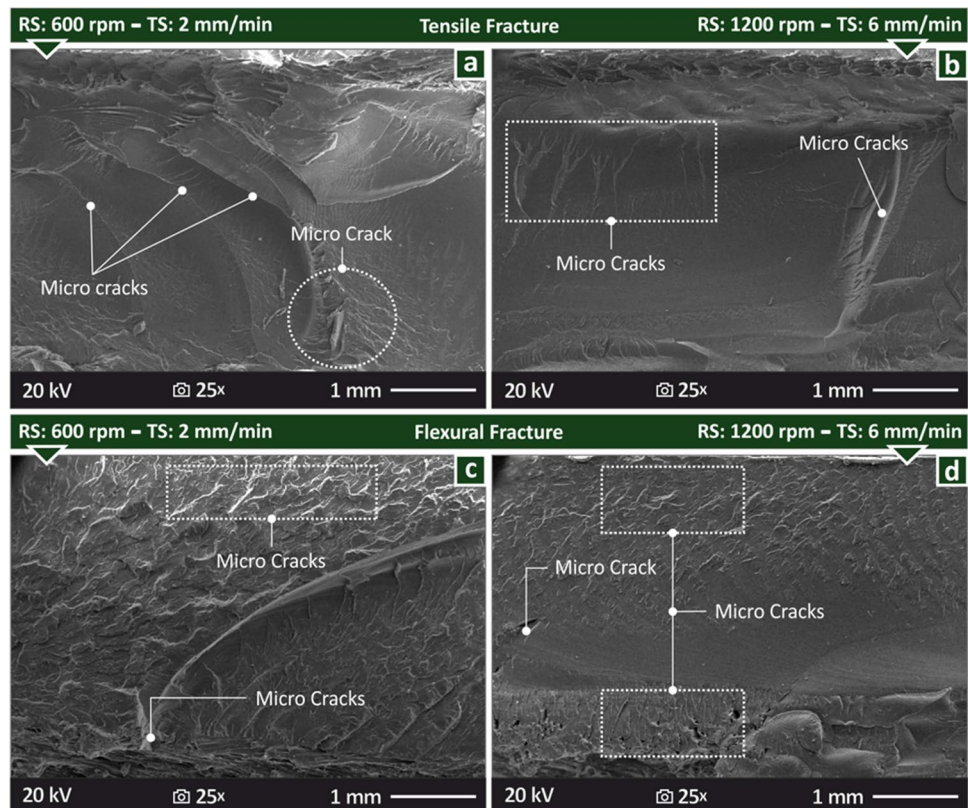
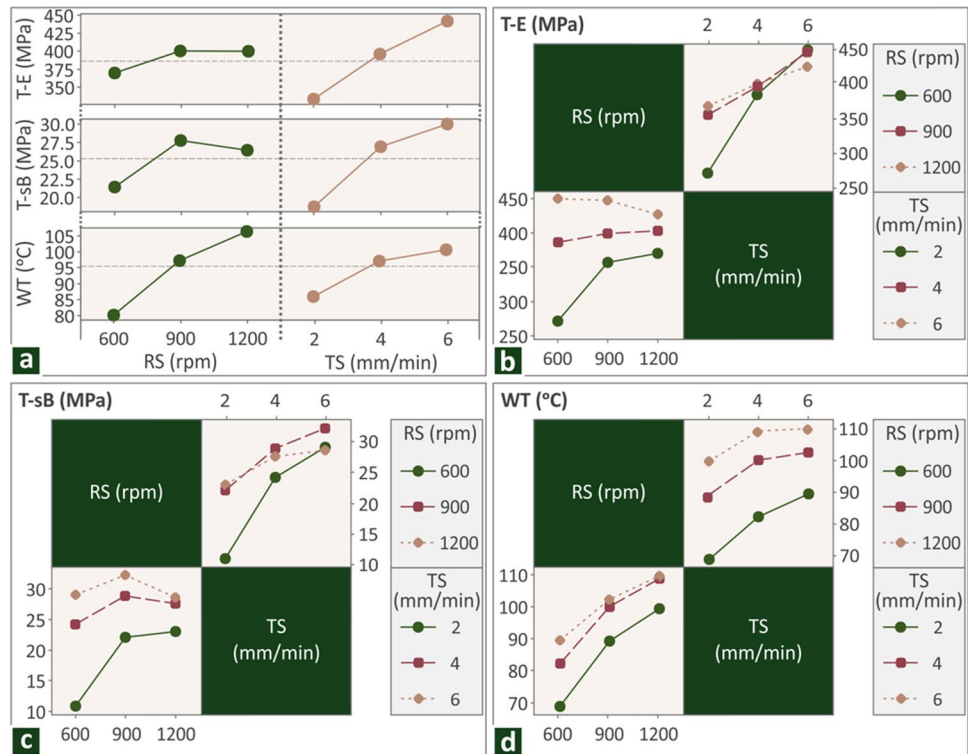


Table 1 Full factorial 3 × 3 design control parameters and levels, average and standard deviations values of measured responses for welding temperature (WT), tensile strength (T-sB), flexural strength (F-sB), tensile modulus of elasticity (T-E), and flexural modulus of elasticity (F-E) for each Experimental run

Run	RS	TS	WT (°C)	T-sB (MPa)	F-sB (MPa)	T-E (MPa)	F-E (MPa)
1	600	2	68.73 ± 2.36	10.90 ± 3.57	26.57 ± 2.54	272.01 ± 60.44	2118.45 ± 18.09
2	600	4	82.20 ± 7.16	24.25 ± 1.33	22.97 ± 6.95	386.15 ± 5.29	2169.67 ± 179.21
3	600	6	89.30 ± 7.41	29.13 ± 2.50	38.59 ± 1.84	449.70 ± 7.03	3301.89 ± 160.54
4	900	2	89.10 ± 3.84	22.14 ± 1.92	28.98 ± 0.58	357.19 ± 12.07	2642.73 ± 44.65
5	900	4	100.10 ± 7.01	28.89 ± 0.52	36.59 ± 2.90	399.05 ± 3.82	2631.43 ± 177.43
6	900	6	102.33 ± 4.62	32.25 ± 2.17	47.96 ± 0.97	446.67 ± 9.79	3464.85 ± 73.23
7	1200	2	99.37 ± 5.25	23.05 ± 3.51	37.84 ± 3.91	369.50 ± 15.88	3604.90 ± 586.83
8	1200	4	109.03 ± 3.81	27.60 ± 2.01	44.76 ± 1.31	402.60 ± 3.73	3012.83 ± 51.52
9	1200	6	109.73 ± 7.20	28.64 ± 0.11	54.83 ± 1.69	426.49 ± 3.32	3671.19 ± 254.44

Fig. 11 Tensile tests: **a** main effect plots for T-E, T-sB, and WT, and interaction plots for **b** T-E, **c** T-sB, and **d** WT



indicate that the prediction models are more than sufficient for the calculation of the corresponding metrics.

$$WT = -22.2 + 0.1426 \times RS + 15.54 \times TS - 0.000046 \times RS^2 - 1.004 \times TS^2 - 0.00425 \times RS \times TS \tag{2}$$

$$T-sB = -53.02 + 0.1060 \times RS + 12.69 \times TS - 0.000043 \times RS^2 - 0.641 \times TS^2 - 0.00526 \times RS \times TS \tag{3}$$

$$F-sB = 16.9 + 0.0241 \times RS - 6.57 \times TS - 0.000003 \times RS^2 + 1.088 \times TS^2 + 0.00207 \times RS \times TS \tag{4}$$

$$T-E = -112.5 + 0.583 \times RS + 90.3 \times TS - 0.000184 \times RS^2 - 2.25 \times TS^2 - 0.0503 \times RS \times TS \tag{5}$$

$$F-E = 1563 + 2.02 \times RS - 467 \times TS + 0.00074 \times RS^2 + 132.3 \times TS^2 - 0.465 \times RS \times TS \tag{6}$$

To identify the statistically important parameters, Pareto charts were formed for each metric and are presented in Fig. 13 and the supplementary material provided. Next to each Pareto chart, a chart with a comparison between the actual (experimental) and the predicted (calculated) values is provided. To evaluate the performance of the prediction

Fig. 12 Flexural tests: **a** main effect plots for F-E, F-sB, and WT, and interaction plots for **b** F-E, **c** F-sB, and **d** WT

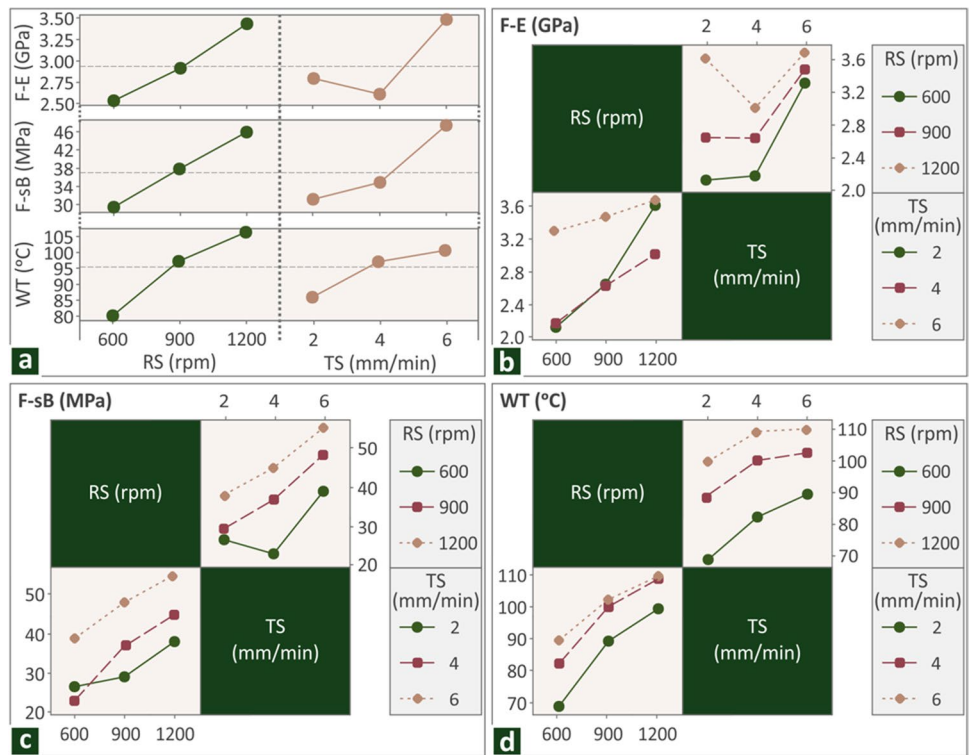


Table 2 Polynomial ANOVA, welding temperature vs RS, TS

Source	DF	Adj SS	Adj MS	F-value	P-value
Regression	5	4286.07	857.213	30.59	0.000
RS	1	286.50	286.500	10.22	0.004
TS	1	278.16	278.159	9.93	0.005
RS ²	1	101.68	101.682	3.63	0.071
TS ²	1	96.80	96.802	3.45	0.077
RS×TS	1	78.03	78.030	2.78	0.110
Error	21	588.51	28.024		
Total	26	4874.58	885.237		
R ²		87.93%			
R ² (adj)		85.05%			
R ² (pred)		79.72%			

Table 3 Polynomial ANOVA, tensile strength vs RS, TS

Source	DF	Adj SS	Adj MS	F-value	P-value
Regression	5	935.18	187.035	38.03	0.00
RS	1	158.33	158.334	32.19	0.00
TS	1	185.44	185.445	37.71	0.00
RS ²	1	88.08	88.077	17.91	0.00
TS ²	1	39.39	39.390	8.01	0.01
RS×TS	1	119.64	119.638	24.33	0.00
Error	21	103.28	4.918		
Total	26	1038.46	191.953		
R ²		90.05%			
R ² (adj)		87.69%			
R ² (pred)		82.71%			

models in the calculation of the response indicators, two metrics were calculated, the mean absolute percentage error (MAPE) [79] and the Durbin-Watson factor [80]. In all cases, the MAPE values indicated a well-acceptable accuracy of the prediction. Durbin-Watson factor values indicate positive autocorrelation of the results (< 2) for the T-E metric and negative autocorrelation of the results for the T-sB and the WT (> 2). Regarding the Pareto charts, all the parameters were statistically important except RS² and TS² for the T-E metric, all were statistically important for the T-sB metric, and RS and TS were the statistically important ones for the WT metric. Figure 14 presents the effect of the

two control parameters in the five metrics studied in a three-dimensional surface plot.

3.7 Two-axis FSW

The experimental results on the mechanical tests of the hybrid PMMA joint showed that welding 3D-printed and bulk PMMA sheets with the FSW process produces a seam with good strength (weld efficiency higher than 1 in several of the cases studied). The morphological examination revealed a good-quality seam with minimum defects and unwelded regions. The FSW settings used were the optimum

Table 4 Polynomial ANOVA, flexural strength vs RS, TS

Source	DF	Adj SS	Adj MS	F-value	P-value
Regression	5	2499.39	499.877	37.73	0.000
RS	1	8.21	8.210	0.62	0.440
TS	1	49.75	49.751	3.75	0.066
RS ²	1	0.38	0.380	0.03	0.867
TS ²	1	113.71	113.709	8.58	0.008
RS×TS	1	18.53	18.526	1.40	0.250
Error	21	278.24	13.249		
Total	26	2777.63	513.126		
R ²		89.98%			
R ² (adj)		87.60%			
R ² (pred)		83.79%			

Table 5 Polynomial ANOVA, tensile modulus of elasticity vs RS, TS

Source	DF	Adj SS	Adj MS	F-value	P-value
Regression	5	69,714.0	13,942.8	28.83	0.000
RS	1	4783.4	4783.4	9.89	0.005
TS	1	9391.4	9391.4	19.42	0.000
RS ²	1	1644.8	1644.8	3.40	0.079
TS ²	1	486.8	486.8	1.01	0.327
RS×TS	1	10,926.4	10,926.4	22.59	0.000
Error	21	10,155.3	483.6		
Total	26	79,869.3	14,426.4		
R ²		87.29%			
R ² (adj)		84.26%			
R ² (pred)		77.04%			

Table 6 Polynomial ANOVA, flexural modulus of elasticity vs RS, TS

Source	DF	Adj SS	Adj MS	F-value	P-value
Regression	5	8,432,512	1,686,502	32.25	0.000
RS	1	57,759	57,759	1.10	0.305
TS	1	251,380	251,380	4.81	0.040
RS ²	1	26,790	26,790	0.51	0.482
TS ²	1	1,681,318	1,681,318	32.15	0.000
RS × TS	1	936,013	936,013	17.90	0.000
Error	21	1,098,073	52,289		
Total	26	9,530,585	1,738,791		
R ²		88.48%			
R ² (adj)		85.74%			
R ² (pred)		79.26%			

ones for welding 3D-printed PMMA parts [10] and worked well in this hybrid joint scenario, too. To further evaluate the feasibility of producing hybrid PMMA joints, two-axis joint schemes were tested. In these tests, all the possible

planar shapes were evaluated, i.e., single- and two-axis paths (linear, curvilinear, acute, right, and obtuse angles, and combinations of those), as mentioned above. Three different joints were designed to include these geometrical shapes and are shown in Fig. 15. The joints were designed (Fig. 15a, d, and g) and manufactured with 3D-printing and bulk PMMA sheets, respectively (Fig. 15b, e, and h). They were assembled to test the fitting of the parts and then they were welded with the FSW process, using the conditions that had the highest mechanical strength in the corresponding experiments (RS 700 rpm and TS 4 mm/min). The produced seam in all three joints is presented in Fig. 15c, f, and i, respectively.

During the FSW process, the temperature was also monitored and the temperature distribution along the seam for all three joints is presented using a color code in Fig. 16a, b, and c. As shown, temperatures along the seam were rather low in the area of 110 °C. Higher temperatures were developed in the angles and especially in the acute angles, in which temperature reached almost 170 °C. This is a higher temperature than the highest reported in the linear seam, in which the temperature did not exceed 150 °C (Fig. 6). This finding by itself justifies the need for such an investigation on the performance of the weld in the two-axis scheme. Still, since the melting temperature of the PMMA was found to be 194 °C, the highest temperature developed in the two-axis joints was much lower than the melting point temperature, verifying that also these seams were produced with the materials in solid state, which is the desired material status for the FSW process.

After the completion of the FSW process, the morphology of the two-axis seam was inspected with an optical stereoscope at six distinct positions indicated in Fig. 16a, b, and c, respectively, for each one of the three different joints tested. The images taken at each position for each joint are presented in Fig. 16. In all images a defect-free seam is presented. Differences can be observed in the roughness of the seam, with images on right angles and along the curvilinear segment of the seam being less rough than in the other positions.

4 Discussion

PMMA has been investigated for its performance in FSW joints in bulk [67, 81] and 3D-printed form [10], with research still being marginal in the field. Dissimilar joints with PMMA sheets and aluminum or other polymers (ABS, etc.) have also been presented [82–85]. Herein, the ability to create a hybrid joint combining 3D-printed and bulk PMMA sheets was proven. Joining PMMA sheets with 3D-printing exploits the ability of 3D printing to construct complex geometry for extending the functionality and applications of

Fig. 13 Pareto chart and actual vs. predicted values for **a** T-E, **b** T-sB, and **c** WT

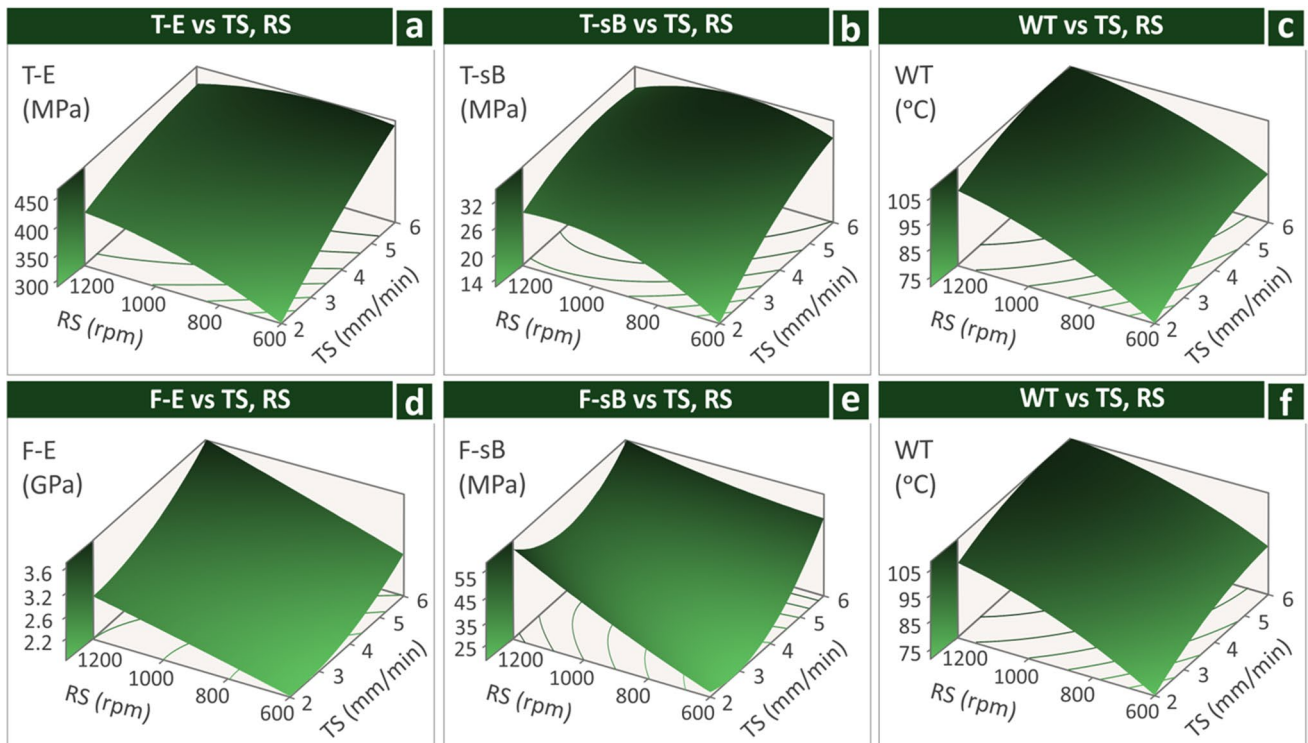
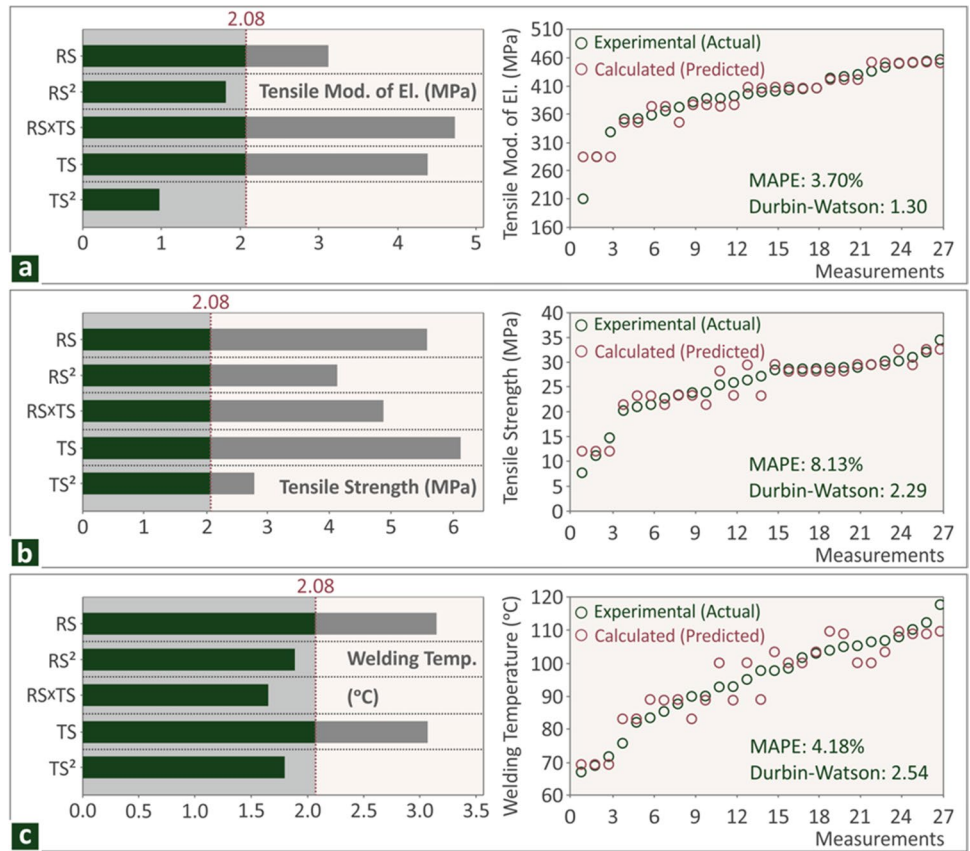


Fig. 14 Surface graphs of the response indicators vs. the TS and RS control parameters **a** T-E, **b** T-sB, **c** WT, **d** F-E, **e** F-sB, and **f** WT

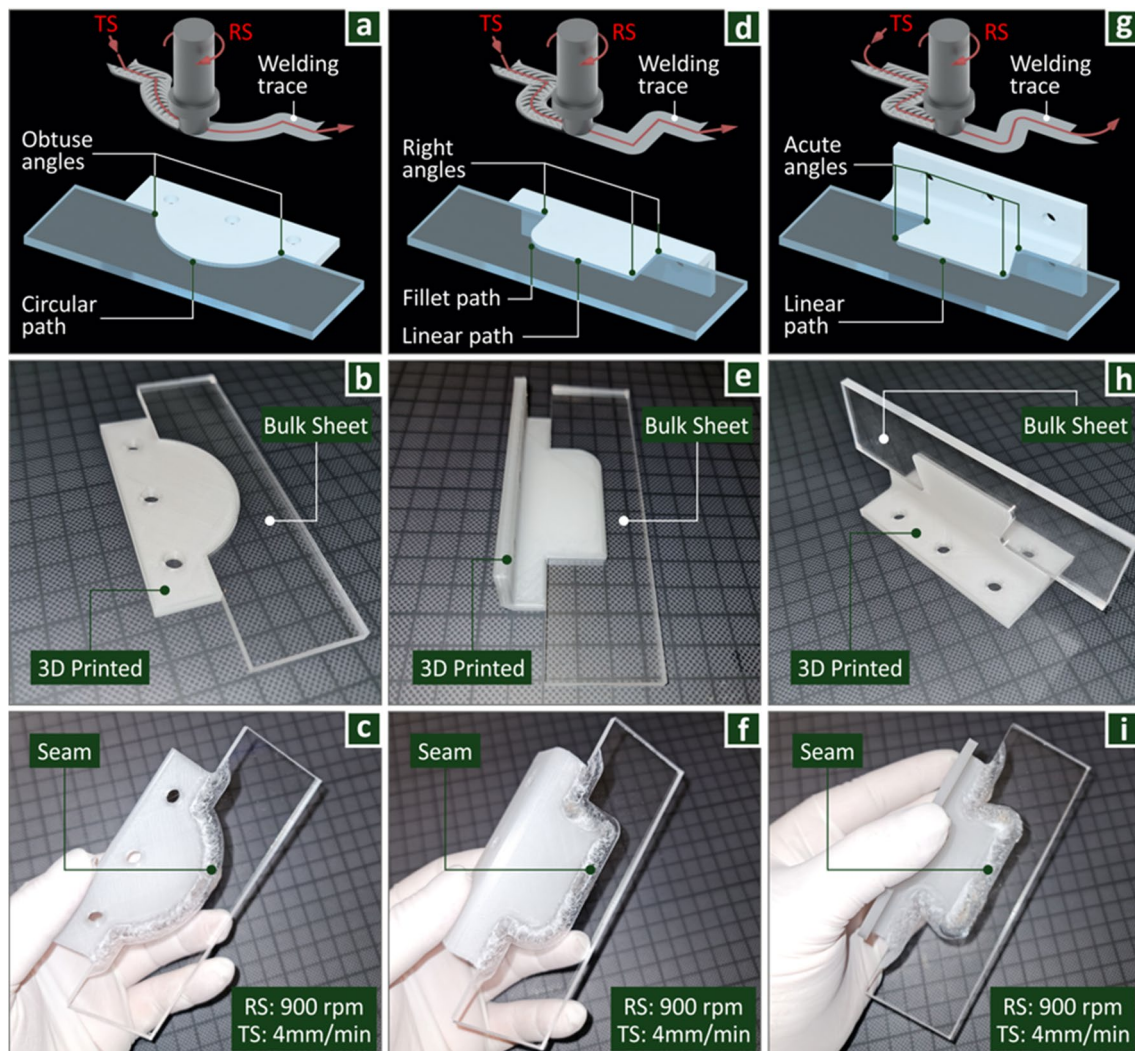


Fig. 15 Two-axis FSW showing the different seam shapes considered herein. The geometry is shown in the first row, the samples prepared and fitted for the process (3D printed and bulk PMMA) are shown in the second row, and in the third row, the completed seam after the joining of the components is presented for each different seam geom-

etries, respectively: **a–c** circular path and obtuse angles, **d–f** linear path, right angles and fillet path, **g–i** linear path and acute angles. In all cases, samples were processed with 900 rpm RS and 4 mm/min TS

the PMMA sheets. As mentioned, the 3D-printing and FSW settings were acquired from the previous study on the FSW of 3D-printed PMMA sheets [10]. The optimum conditions according to the statistical analysis conducted in this study were used herein. Due to these optimized settings used, good quality seams were achieved, with good morphological characteristics and strength. Welding efficiency higher than 1 was achieved in most cases, compared to PMMA 3D-printed parts. The highest welding efficiency reported was 1.36 in the tensile tests, achieved by the sample welded with 900 rpm and 6 mm/min FSW conditions. The sample welded with the same conditions achieved also the highest welding efficiency in the flexural tests, which was 0.98, also a more than sufficient value for welding efficiency. Still, two

control parameters (RS and TS) with three levels each were investigated. The results showed the importance of the FSW parameters in the performance of the weld and the use of statistical modeling tools for the analysis of the experimental results. The difference in the tensile strength of hybrid joint specimens welded with different FSW settings reached 35%. It should be noted that while experimental results showed improvement in processing quality, heat input or generated heat during friction stir welding has a significant role in the thermal properties, the width of weld samples, morphology of the sample, mechanical characteristics, and weld efficiency of samples [86–88] affecting the reported results. Deepening the investigation into these parameters can be a subject of future work.

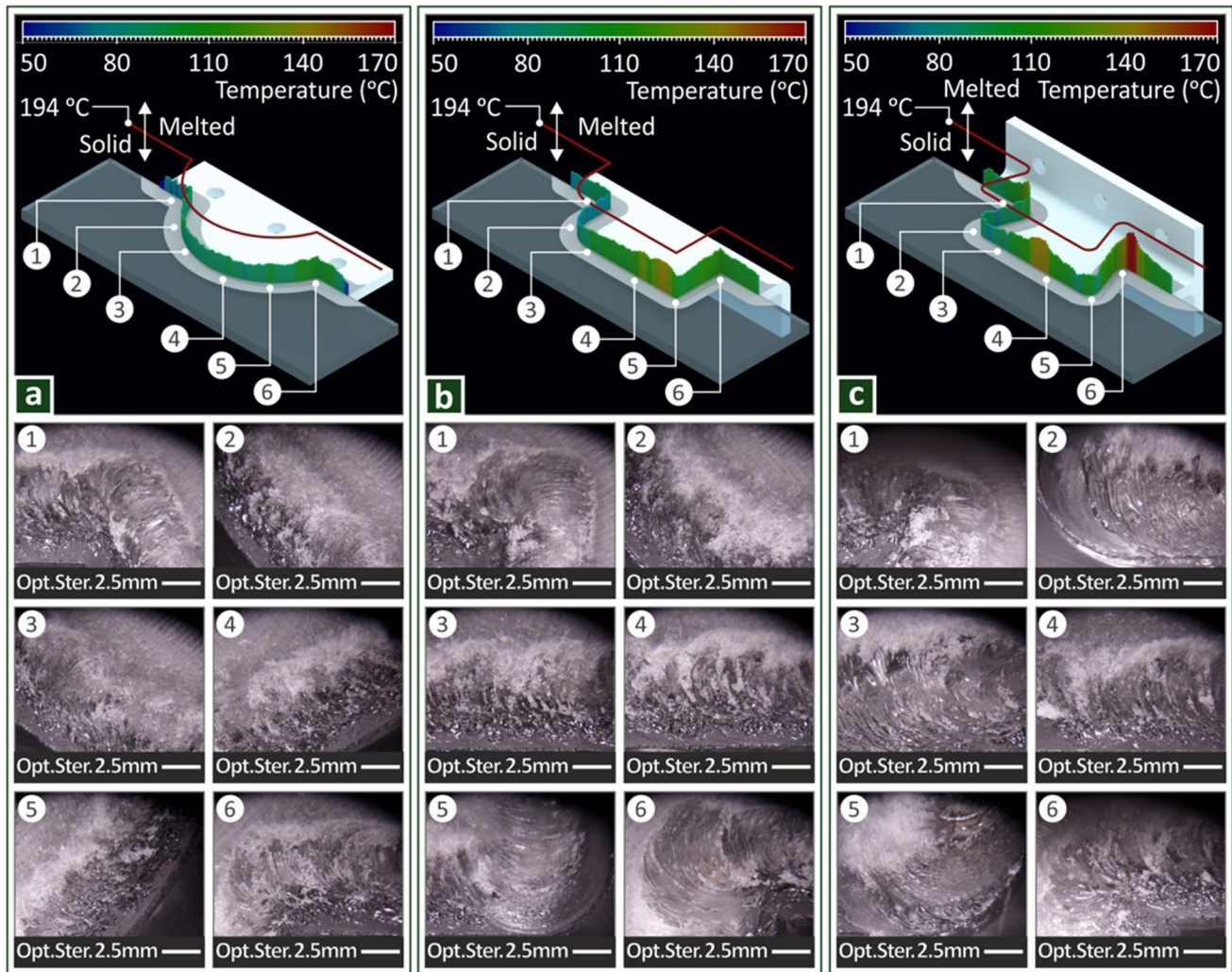


Fig. 16 The top images show with a color bar the temperature developed along the seam during the FSW process in the three different seam shapes performed: **a** circular path and obtuse angles; **b** linear path, right angles, and fillet path; **c** linear path and acute angles. Below each image, stereoscopic images at the six seam regions indi-

cated on the top image are presented, depicting the morphology along the seam at positions with different seam geometries. The 194 °C temperature shown is the melting temperature of the PMMA, so recorded temperatures (< 170 °C) verify the solid state of the process

It should be noted that the bulk sheet has a solid structure, while the 3D-printed structure has voids and porosity [70]. The layers' shape is not always uniform [89] and the strength of the performance of the parts is affected by the bonding between the strands [90]. Due to these characteristics, 3D-printed parts show anisotropy [91, 92] and inferior mechanical properties compared to bulk sheet parts [93, 94]. Such differences in the properties and the structure of the 3D-printed parts compared to the bulk sheet parts justify why the feasibility of such hybrid joints is a challenging task and why the investigation of the performance of such hybrid joints has industrial and scientific merit.

Additionally, since FSW is a process in which the material should be in a solid state [95], one of the aspects highly affecting the feasibility of the process is the material flow

caused by the temperature increase occurring during the process. As expected, how the material flow is affected by the temperature has been investigated for the FSW process, mainly in alloys [96–98]. As the temperature increases, the material flow of the material is increased, improving the stirring of the materials and facilitating the FSW process to perform a weld. The effect of temperature in the process performed in the current study is presented in the MEP (Figs. 11 and 12). The increase of the temperature increases the mechanical properties, verifying the argument that as the temperature increases, the material flow is increased and the mixing of the materials is improved, leading to more robust welds. In the current study, the average temperature per case studied is ranging from 80 to 105 °C. Both the increase of the RS and the TS increase the temperature during the FSW

process and this has a positive effect on the performance of the welds, verifying the aforementioned argument.

The merit of the two-axis welding scenarios studied was also proven, since an increase in the temperature of up to 12% was found, especially in the acute angles. The maximum temperature recorded was up to 170 °C. This temperature is lower than 194 °C, which is the melting point, still, it is closer to it than the 150 °C which was the temperature recorded in the linear welding scenario of the hybrid joint. So, the shape of the seam should be considered also to ensure that the solid state of the materials is maintained throughout the FSW process. It should be noted also that the temperatures reported for the linear seam are in good agreement with the literature on joining bulk PMMA sheets [67].

Results in the mechanical tests presented herein cannot be directly correlated with the literature, since no similar joint has been presented yet to the authors' best knowledge. Comparing the results with the corresponding ones for welding PMMA 3D-printed parts [10], the highest strength achieved on the hybrid PMMA joint in the tensile test is more than 100% higher than the 3D-printing joint (approximately 46 MPa vs. approximately 20 MPa). A study on the FSW of bulk PMMA sheets welded with higher RS than the ones used herein reported the tensile strength of the welded sheets up to approximately 57 MPa [67]. The lowest tensile strength reported in this study was approximately 37 MPa. Such differences are expected since the 3D-printed parts welded herein have inferior strength than the bulk sheets and this affects the performance of the hybrid joint. Still, it provides the ability to join complex geometry parts on the PMMA sheets. Additionally, it should be noted that in this study [67], the increase in the RS also resulted in higher-strength joints, similar to the findings presented herein. The other study on joining bulk PMMA sheets with the FSW process [81] uses lower RS values than the current study and higher TS. Statistical modeling tools and regression were used, still, the results cannot be compared with the current findings since the authors provide results in force units and not in stress units.

5 Conclusions

Herein, the feasibility of producing hybrid joints by welding 3D-printed and bulk PMMA sheets with the FSW process was proven. An FFD approach was used with two control parameters (RS and TS) and three levels each. Tensile and flexural tests were conducted, along with microhardness measurements, while the thermal properties of the PMMA grade used were determined. Weld efficiency higher than 1 was achieved by all joints, except the ones welded with 2 mm/min TS, showing the importance of the weld conditions in the performance of the weld. The highest welding

efficiency was achieved in the tensile tests (1.36) by a sample welded with 900 rpm and 6 mm/min. In the flexural tests, the highest welding efficiency was achieved by a sample welded with the same conditions. A 0.98 welding efficiency was reported, which is more than sufficient achievement.

The increase of TS increased the mechanical strength of the hybrid joints (a more than 30% difference is reported between the sample welded with lower and high TS values), while the increase of RS had in most cases a similar effect. The morphological examination revealed a good-quality seam with minimum cavities and defects, while the thermal property examination verified the solid state of the materials during the FSW process. Regression analysis provided prediction models for the five metrics studied, i.e., WT, T-sB, T-E, F-sB, and F-E. To further evaluate the feasibility of the hybrid PMMA joint, planar two-axis joints were implemented. It was found that the quality of the seam is maintained even in these case scenarios; still, the developed temperatures are higher, especially in the acute angles. Such hybrid joints significantly extend the functionality of the PMMA sheets and the applicability of the 3D-printing process and have direct industrial application. In future work, dissimilar material hybrid joints can be tested, along with more sophisticated modeling tools and additional control parameters.

Supplementary Information The online version contains supplementary material available at <https://doi.org/10.1007/s00170-023-11632-6>.

Acknowledgements The authors would like to thank Aleka Manousaki from the Institute of Electronic Structure and Laser of the Foundation for Research and Technology, Hellas (IESL-FORTH), for taking the SEM images presented in this work.

Author contribution Markos Petousis: methodology, formal analysis, writing—original draft preparation, writing—review, and editing; Nikolaos Mountakis: software, formal analysis, investigation, and data curation; Nectarios Vidakis: conceptualization, methodology, resources, supervision, and project administration. The manuscript was written through the contributions of all authors. All authors have approved the final version of the manuscript.

Funding Open access funding provided by HEAL-Link Greece.

Data availability The raw/processed data required to reproduce these findings cannot be shared at this time due to technical or time limitations.

Declarations

Competing interests The authors declare no competing interests.

Open Access This article is licensed under a Creative Commons Attribution 4.0 International License, which permits use, sharing, adaptation, distribution and reproduction in any medium or format, as long as you give appropriate credit to the original author(s) and the source, provide a link to the Creative Commons licence, and indicate if changes were made. The images or other third party material in this article are included in the article's Creative Commons licence, unless indicated

otherwise in a credit line to the material. If material is not included in the article's Creative Commons licence and your intended use is not permitted by statutory regulation or exceeds the permitted use, you will need to obtain permission directly from the copyright holder. To view a copy of this licence, visit <http://creativecommons.org/licenses/by/4.0/>.

References

- Mani M, Witherell P, Jee H (2017) design rules for additive manufacturing: a categorization. Proceedings of the ASME 2017 International Design Engineering Technical Conferences and Computers and Information in Engineering Conference. Volume 1: 37th Computers and Information in Engineering Conference. Cleveland, Ohio, USA. V001T02A035. ASME. <https://doi.org/10.1115/DETC2017-68446>
- Ziółkowski M, Dyl T (2020) Possible applications of additive manufacturing technologies in shipbuilding: a review. *Machines* 8:1–34. <https://doi.org/10.3390/machines8040084>
- Pereira T, Kennedy JV, Potgieter J (2019) A comparison of traditional manufacturing vs additive manufacturing, the best method for the job. *Procedia Manuf* 30:11–18. <https://doi.org/10.1016/j.promfg.2019.02.003>
- Kumar S (2022) Disadvantage BT - additive manufacturing solutions. In: International Springer (ed) Kumar S. Publishing, Cham, pp 31–40
- Kechagias JD, Fountas NA, Ninikas K et al (2022) Surface characteristics investigation of 3D-printed PET-G plates during CO2 laser cutting. *Mater Manuf Process* 37:1347–1357. <https://doi.org/10.1080/10426914.2021.1981933>
- Kechagias JD, Ninikas K, Petousis M, Vidakis N (2022) Laser cutting of 3D printed acrylonitrile butadiene styrene plates for dimensional and surface roughness optimization. *J Adv Manuf Technol* 119:2301–2315. <https://doi.org/10.1007/s00170-021-08350-2>
- Kechagias JD, Vidakis N, Ninikas K et al (2022) Hybrid 3D printing of multifunctional polylactic acid / carbon black nanocomposites made with material extrusion and post - processed with CO 2 laser cutting. *Int J Adv Manuf Technol*. <https://doi.org/10.1007/s00170-022-10604-6>
- Petousis M, Ninikas K, Vidakis N et al (2023) Multifunctional PLA/CNTs nanocomposites hybrid 3D printing integrating material extrusion and CO2 laser cutting. *J Manuf Process* 86:237–252. <https://doi.org/10.1016/j.jmapro.2022.12.060>
- Vidakis N, Petousis M, Mountakis N, Kechagias JD (2022) Optimization of friction stir welding for various tool pin geometries : the weldability of Polyamide 6 plates made of material extrusion additive manufacturing. *Int J Adv Manuf* 6(4):77. <https://doi.org/10.3390/jmmp6040077>
- Vidakis N, Petousis M, Mountakis N, Kechagias JD (2022) Optimization of friction stir welding parameters in hybrid additive manufacturing: weldability of 3D-printed poly(methyl methacrylate) Plates. *J Manuf Mater Process* 6. <https://doi.org/10.3390/jmmp6040077>
- Vidakis N, Petousis M, Mountakis N, Kechagias JD (2022) Material extrusion 3D printing and friction stir welding: an insight into the weldability of polylactic acid plates based on a full factorial design. *Int J Adv Manuf Technol* 121:3817–3839. <https://doi.org/10.1007/s00170-022-09595-1>
- Sheikh-Ahmad JY, Ali DS, Devenci S et al (2019) Friction stir welding of high density polyethylene—carbon black composite. *J Mater Process Technol* 264:402–413. <https://doi.org/10.1016/j.jmatprotec.2018.09.033>
- Vidakis N, Petousis M, Korlos A et al (2022) Friction stir welding optimization of 3D-printed acrylonitrile butadiene styrene in hybrid additive manufacturing. *Polymers (Basel)* 14:2474. <https://doi.org/10.3390/polym14122474>
- Singh S, Prakash C, Gupta MK (2020) On friction-stir welding of 3D printed thermoplastics. *Springer, Cham* 75–91. https://doi.org/10.1007/978-3-030-18854-2_3
- Dimopoulos A, Vairis A, Vidakis N, Petousis M (2021) On the friction stir welding of al 7075 thin sheets. *Metals (Basel)* 11:1–12. <https://doi.org/10.3390/met11010057>
- Çam G (2011) Friction stir welded structural materials: beyond Al-alloys. *Int Mater Rev* 56:1–48. <https://doi.org/10.1179/095066010X12777205875750>
- Saeid T, Abdollah-zadeh A, Sazgari B (2010) Weldability and mechanical properties of dissimilar aluminum–copper lap joints made by friction stir welding. *J Alloys Compd* 490:652–655. <https://doi.org/10.1016/j.jallcom.2009.10.127>
- Vidakis N, Vairis A, Diouf D et al (2012) Effect of the tool rotational speed on the mechanical properties of thin AA1050 friction stir welded sheets. *Eng Sci Technol Rev* 5:9–13
- Wu D, Li W, Gao Y et al (2021) Impact of travel speed on the microstructure and mechanical properties of adjustable-gap bobbin-tool friction stir welded Al-Mg joints. *Int J Miner Metall Mater* 28:710–717. <https://doi.org/10.1007/s12613-020-2134-9>
- Chien CH, Lin WB, Chen T (2011) Optimal FSW process parameters for aluminum alloys AA5083. *J Chinese Inst Eng Trans Chinese Inst Eng A* 34:99–105. <https://doi.org/10.1080/02533839.2011.553024>
- Heinz B, Skrotzki B (2002) Characterization of a friction-stir-welded aluminum alloy 6013. *Metall Mater Trans B* 33:489–498. <https://doi.org/10.1007/s11663-002-0059-5>
- Sakthivel T, Sengar GS, Mukhopadhyay J (2009) Effect of welding speed on microstructure and mechanical properties of friction-stir-welded aluminum. *Int J Adv Manuf Technol* 43:468–473. <https://doi.org/10.1007/s00170-008-1727-7>
- Fujii H, Cui L, Maeda M, Nogi K (2006) Effect of tool shape on mechanical properties and microstructure of friction stir welded aluminum alloys. *Mater Sci Eng A* 419:25–31. <https://doi.org/10.1016/j.msea.2005.11.045>
- Mironov S, Inagaki K, Sato YS, Kokawa H (2015) Effect of welding temperature on microstructure of friction-stir welded aluminum alloy 1050. *Metall Mater Trans A* 46:783–790. <https://doi.org/10.1007/s11661-014-2651-0>
- Li H, Gao J, Li Q (2018) Fatigue of friction stir welded aluminum alloy joints: a review. *Appl Sci* 8:2626. <https://doi.org/10.3390/app8122626>
- Ghangas G, Singhal S, Dixit S et al (2022) Mathematical modeling and optimization of friction stir welding process parameters for armor-grade aluminium alloy. *Int J Interact Des Manuf*. <https://doi.org/10.1007/s12008-022-01000-1>
- Zamrudi FH, Setiawan AR (2022) Effect of friction stir welding parameters on corrosion behaviour of aluminium alloys: an overview. *Corros Eng Sci Technol* 57(7):696–707. <https://doi.org/10.1080/1478422X.2022.2116185>
- Antoniadis A, Vidakis N, Bilalis N (2002) Fatigue fracture investigation of cemented carbide tools in gear hobbing, Part 2: the effect of cutting parameters on the level of tool stresses - a quantitative parametric analysis. *J Manuf Sci Eng* 124:792–798. <https://doi.org/10.1115/1.1511173>
- Balamurugan S, Jayakumar K, Anbarasan B, Rajesh M (2022) Effect of tool pin shapes on microstructure and mechanical behaviour of friction stir welding of dissimilar aluminium alloys. *Mater Today Proc* 72:2181–2185. <https://doi.org/10.1016/j.matpr.2022.08.459>
- Kubit A, Trzepieciński T, Kluz R et al (2022) Multi-criteria optimisation of friction stir welding parameters for EN AW-2024-T3

- aluminium alloy joints. *Materials (Basel)* 15:5428. <https://doi.org/10.3390/ma15155428>
31. Varunraj S, Ruban M (2022) Investigation of the microstructure and mechanical properties of AA6063 and AA7075 dissimilar aluminium alloys by friction stir welding process. *Mater Today Proc.* 68:1654–1657. <https://doi.org/10.1016/j.matpr.2022.08.095>
 32. Abdollahzadeh A, Bagheri B, Abbasi M et al (2021) A modified version of friction stir welding process of aluminum alloys: analyzing the thermal treatment and wear behavior. *Proc Inst Mech Eng Part L J Mater Des Appl* 235:2291–2309. <https://doi.org/10.1177/14644207211023987>
 33. Bagheri B, Abdollahzadeh A, Sharifi F et al (2021) Recent development in friction stir processing of aluminum alloys: microstructure evolution, mechanical properties, wear and corrosion behaviors. *Proc Inst Mech Eng Part E J Process Mech Eng* 0(0):09544089211058007. <https://doi.org/10.1177/09544089211058007>
 34. Abbasi M, Bagheri B, Abdollahzadeh A, Moghaddam AO (2021) A different attempt to improve the formability of aluminum tailor welded blanks (TWB) produced by the FSW. *Int J Mater Form* 14:1189–1208. <https://doi.org/10.1007/s12289-021-01632-w>
 35. Abbasi M, Bagheri B, Sharifi F (2021) Simulation and experimental study of dynamic recrystallization process during friction stir vibration welding of magnesium alloys. *Trans Nonferrous Met Soc China* 31:2626–2650. [https://doi.org/10.1016/S1003-6326\(21\)65681-9](https://doi.org/10.1016/S1003-6326(21)65681-9)
 36. Correia AN, Santos PAM, Braga DFO et al (2023) Effects of processing temperature on failure mechanisms of dissimilar aluminum-to-polymer joints produced by friction stir welding. *Eng Fail Anal* 146:107155. <https://doi.org/10.1016/j.engfailanal.2023.107155>
 37. Singh VP, Kumar R, Kumar A, Dewangan AK (2023) Automotive light weight multi-materials sheets joining through friction stir welding technique: an overview. *Mater Today Proc.* <https://doi.org/10.1016/j.matpr.2023.02.171>. (in press)
 38. Ali U, Karim KJBA, Buang NA (2015) A Review of the Properties and Applications of Poly (Methyl Methacrylate) (PMMA). *Polym Rev* 55:678–705. <https://doi.org/10.1080/15583724.2015.1031377>
 39. Zidan HM, Abu-Elnader M (2005) Structural and optical properties of pure PMMA and metal chloride-doped PMMA films. *Phys B Condens Matter* 355:308–317. <https://doi.org/10.1016/j.physb.2004.11.023>
 40. Ochoa NA, Masuelli M, Marchese J (2003) Effect of hydrophilicity on fouling of an emulsified oil wastewater with PVDF/PMMA membranes. *J Memb Sci* 226:203–211. <https://doi.org/10.1016/j.memsci.2003.09.004>
 41. Zheng W, Wong SC (2003) Electrical conductivity and dielectric properties of PMMA/expanded graphite composites. *Compos Sci Technol* 63:225–235. [https://doi.org/10.1016/S0266-3538\(02\)00201-4](https://doi.org/10.1016/S0266-3538(02)00201-4)
 42. Sari A, Alkan C, Biçer A et al (2014) Micro/nanoencapsulated n-nonadecane with poly(methyl methacrylate) shell for thermal energy storage. *Energy Convers Manag* 86:614–621. <https://doi.org/10.1016/j.enconman.2014.05.092>
 43. Meng Q, Li W, Zheng Y, Zhang Z (2010) Effect of poly(methyl methacrylate) addition on the dielectric and energy storage properties of poly(vinylidene fluoride). *J Appl Polym Sci* 116:2674–2684. <https://doi.org/10.1002/app.31777>
 44. Gupta R, Kumar V, Goyal PK, Kumar S (2012) Optical characterization of poly(methyl methacrylate) implanted with low energy ions. *Appl Surf Sci* 263:334–338. <https://doi.org/10.1016/j.apsusc.2012.09.056>
 45. Zhu Y, Jiang P, Huang X (2019) Poly(vinylidene fluoride) terpolymer and poly(methyl methacrylate) composite films with superior energy storage performance for electrostatic capacitor application. *Compos Sci Technol* 179:115–124. <https://doi.org/10.1016/j.compscitech.2019.04.035>
 46. Chi Q, Zhou Y, Yin C et al (2019) A blended binary composite of poly(vinylidene fluoride) and poly(methyl methacrylate) exhibiting excellent energy storage performances. *J Mater Chem C* 7:14148–14158. <https://doi.org/10.1039/C9TC04695J>
 47. Morales-Gómez JA, Garcia-Estrada E, Leos-Bortoni JE et al (2019) Cranioplasty with a low-cost customized polymethylmethacrylate implant using a desktop 3D printer. *J Neurosurg JNS* 130:1721–1727. <https://doi.org/10.3171/2017.12.JNS172574>
 48. Petersmann S, Spoerk M, Huber P et al (2019) Impact optimization of 3D-printed poly(methyl methacrylate) for cranial implants. *Macromol Mater Eng* 304:1900263. <https://doi.org/10.1002/mame.201900263>
 49. Scerrati A, Travaglini F, Gelmi CAE et al (2022) Patient specific polymethyl methacrylate customised cranioplasty using 3D printed silicone moulds: technical note. *Int J Med Robot Comput Assist Surg* 18:e2353. <https://doi.org/10.1002/rsc.2353>
 50. Caro-Osorio E, De la Garza-Ramos R, Martínez-Sánchez SR, Olazarán-Salinas F (2013) Cranioplasty with polymethylmethacrylate prostheses fabricated by hand using original bone flaps: technical note and surgical outcomes. *Surg Neurol Int* 4:136. <https://doi.org/10.4103/2152-7806.119535>
 51. Chamo D, Msallem B, Sharma N et al (2020) Accuracy assessment of molded, patient-specific polymethylmethacrylate craniofacial implants compared to their 3D printed originals. *J Clin Med* 9:832
 52. de Oliveira Limírio JPI, de Gomes JML, Alves Rezende MCR et al (2022) Mechanical properties of polymethyl methacrylate as a denture base: Conventional versus CAD-CAM resin – a systematic review and meta-analysis of in vitro studies. *J Prosthet Dent* 128:1221–1229. <https://doi.org/10.1016/j.prosdent.2021.03.018>
 53. Salgado H, Gomes ATPC, Duarte AS et al (2022) Antimicrobial activity of a 3D-printed polymethylmethacrylate dental resin enhanced with graphene. *Biomedicine* 10:2607
 54. Feuser PE, Gaspar PC, Ricci-Júnior E et al (2014) Synthesis and characterization of poly(methyl methacrylate) pmma and evaluation of cytotoxicity for biomedical application. *Macromol Symp* 343:65–69. <https://doi.org/10.1002/masy.201300194>
 55. Vidakis N, Petousis M, Velidakis E et al (2022) Mechanical reinforcement course of 3D printed polypropylene–antimony doped tin oxide nanocomposites versus filler loading. *Adv Compos Mater* 31:235–256. <https://doi.org/10.1080/09243046.2021.1973173>
 56. Vidakis N, Petousis M, Velidakis E et al (2022) Multi-functional polyamide 12 (PA12)/ multiwall carbon nanotube 3D printed nanocomposites with enhanced mechanical and electrical properties. *Adv Compos Mater* 31:630–654. <https://doi.org/10.1080/09243046.2022.2076019>
 57. Vidakis N, Maniadi A, Petousis M et al (2020) Mechanical and electrical properties investigation of 3D-printed acrylonitrile–butadiene–styrene graphene and carbon nanocomposites. *J Mater Eng Perform* 29:1909–1918. <https://doi.org/10.1007/s11665-020-04689-x>
 58. Vidakis N, Petousis M, Velidakis E et al (2020) On the strain rate sensitivity of fused filament fabrication (Fff) processed pla, abs, petg, pa6, and pp thermoplastic polymers. *Polymers (Basel)* 12:1–15. <https://doi.org/10.3390/polym12122924>
 59. Polzin C, Spath S, Seitz H (2013) Characterization and evaluation of a PMMA-based 3D printing process. *Rapid Prototyp J* 19:37–43. <https://doi.org/10.1108/13552541311292718>
 60. Chen S-GG, Yang J, Jia Y-GG et al (2019) Tio2 and PEEK reinforced 3d printing pmma composite resin for dental denture base applications. *Nanomaterials* 9(7):1049. <https://doi.org/10.3390/nano9071049>

61. Dimitrova M, Corsalini M, Kazakova R et al (2022) Comparison between conventional PMMA and 3D printed resins for denture bases: a narrative review. *J Compos Sci* 6:87. <https://doi.org/10.3390/jcs6030087>
62. Matbouei A, Fathi A, Rabiee SM, Shirzad M (2019) Layered manufacturing of a three-dimensional polymethyl methacrylate (PMMA) scaffold used for bone regeneration. *Mater Technol* 34:167–177. <https://doi.org/10.1080/10667857.2018.1541212>
63. Al-Dwairi ZN, Al Haj Ebrahim AA, Baba NZ (2022) A comparison of the surface and mechanical properties of 3D printable denture-base resin material and conventional polymethylmethacrylate (PMMA). *J Prosthodont* 32:40–48. <https://doi.org/10.1111/jopr.13491>
64. Lourinho C, Salgado H, Correia A, Fonseca P (2022) Mechanical properties of polymethyl methacrylate as denture base material: heat-polymerized vs. 3D-printed—systematic review and meta-analysis of in vitro studies. *Biomedicines* 10:2665
65. Petersmann S, Spoerk M, Van De Steene W et al (2020) Mechanical properties of polymeric implant materials produced by extrusion-based additive manufacturing. *J Mech Behav Biomed Mater* 104:103611. <https://doi.org/10.1016/j.jmbbm.2019.103611>
66. Vidakis N, Petousis M, Mountakis N et al (2023) Energy consumption vs. tensile strength of poly [methyl methacrylate] in material extrusion 3D printing : the impact of six control settings. *Polymers (Basel)* 15:845. <https://doi.org/10.3390/polym15040845>
67. Aghajani Derazkola H, Simchi A (2018) Experimental and thermomechanical analysis of friction stir welding of poly(methyl methacrylate) sheets. *Sci Technol Weld Join* 23:209–218. <https://doi.org/10.1080/13621718.2017.1364896>
68. Elyasi M, Derazkola HA (2018) Experimental and thermo-mechanical study on FSW of PMMA polymer T-joint. *Int J Adv Manuf Technol* 97:1445–1456. <https://doi.org/10.1007/s00170-018-1847-7>
69. Derazkola HA, Kashiry Fard R, Khodabakhshi F (2018) Effects of processing parameters on the characteristics of dissimilar friction-stir-welded joints between AA5058 aluminum alloy and PMMA polymer. *Weld World* 62:117–130. <https://doi.org/10.1007/s40194-017-0517-y>
70. Vidakis N, David C, Petousis M et al (2022) The effect of six key process control parameters on the surface roughness, dimensional accuracy, and porosity in material extrusion 3D printing of polylactic acid : prediction models and optimization supported by robust design analysis. *Adv Ind Manuf Eng* 5:100104. <https://doi.org/10.1016/j.aime.2022.100104>
71. Vidakis N, David CN, Petousis M et al (2022) Optimization of key quality indicators in material extrusion 3D printing of acrylonitrile butadiene styrene: the impact of critical process control parameters on the surface roughness, dimensional accuracy, and porosity. *Mater Today Commun* 34:105171. <https://doi.org/10.1016/j.mtcomm.2022.105171>
72. Sadeghian N, Besharati Givi MK (2015) Experimental optimization of the mechanical properties of friction stir welded acrylonitrile butadiene styrene sheets. *Mater Des* 67:145–153. <https://doi.org/10.1016/j.matdes.2014.11.032>
73. Tarasov SY, Rubtsov VE, Fortuna SV et al (2017) Ultrasonic-assisted aging in friction stir welding on Al-Cu-Li-Mg aluminum alloy. *Weld World* 61:679–690. <https://doi.org/10.1007/s40194-017-0447-8>
74. Song Y, Li Y, Song W et al (2017) Measurements of the mechanical response of unidirectional 3D-printed PLA. *Mater Des* 123:154–164. <https://doi.org/10.1016/j.matdes.2017.03.051>
75. Huang Y, Meng X, Xie Y et al (2018) Friction stir welding/processing of polymers and polymer matrix composites. *Compos Part A Appl Sci Manuf* 105:235–257. <https://doi.org/10.1016/j.compositesa.2017.12.005>
76. Awaja F, Zhang S, Tripathi M et al (2016) Cracks, microcracks and fracture in polymer structures: formation, detection, autonomic repair. *Prog Mater Sci* 83:536–573. <https://doi.org/10.1016/j.pmatsci.2016.07.007>
77. Ravi-Chandar K, Yang B (1997) On the role of microcracks in the dynamic fracture of brittle materials. *J Mech Phys Solids* 45:535–563. [https://doi.org/10.1016/S0022-5096\(96\)00096-8](https://doi.org/10.1016/S0022-5096(96)00096-8)
78. Phadke MS (1995) *Quality engineering using robust design*, 1st edn. Prentice Hall PTR, USA
79. Swamidass PM (Ed. . (2000) MAPE (mean absolute percentage error)mean absolute percentage error (MAPE) BT - encyclopedia of production and manufacturing management. In: Swamidass PM (ed). Springer US, Boston, MA, USA, 462
80. White KJ (1992) The Durbin-Watson test for autocorrelation in nonlinear models. *Rev Econ Stat* 74:370–373. <https://doi.org/10.2307/2109675>
81. Adibeig MR, Hassanifard S, Vakili-Tahami F, Hattel JH (2018) Experimental investigation of tensile strength of friction stir welded butt joints on PMMA. *Mater Today Commun* 17:238–245. <https://doi.org/10.1016/j.mtcomm.2018.09.009>
82. Kumar R, Singh R, Ahuja IPSS et al (2018) Weldability of thermoplastic materials for friction stir welding- a state of art review and future applications. *Compos Part B Eng* 137:1–15. <https://doi.org/10.1016/j.compositesb.2017.10.039>
83. Dalwadi CG, Patel AR, Kapopara JM et al (2018) Examination of mechanical properties for dissimilar friction stir welded joint of Al alloy (AA-6061) to PMMA (acrylic). *Mater Today Proc* 5:4761–4765. <https://doi.org/10.1016/j.matpr.2017.12.049>
84. Zafar A, Awang M, Khan SR (2017) Friction stir welding of polymers: an overview BT - 2nd International Conference on Mechanical, Manufacturing and Process Plant Engineering. In: Awang M (ed). Springer Singapore, Singapore, 19–36
85. Paoletti A, Lambiase F, Di Ilio A (2015) Optimization of friction stir welding of thermoplastics. *Procedia CIRP* 33:562–567. <https://doi.org/10.1016/j.procir.2015.06.078>
86. Abbasi M, Abdollahzadeh A, Bagheri B et al (2021) Study on the effect of the welding environment on the dynamic recrystallization phenomenon and residual stresses during the friction stir welding process of aluminum alloy. *Proc Inst Mech Eng Part L J Mater Des Appl* 235:1809–1826. <https://doi.org/10.1177/14644207211025113>
87. Bagheri B, Sharifi F, Abbasi M, Abdollahzadeh A (2021) On the role of input welding parameters on the microstructure and mechanical properties of Al6061-T6 alloy during the friction stir welding: Experimental and numerical investigation. *Proc Inst Mech Eng Part L J Mater Des Appl* 236:299–318. <https://doi.org/10.1177/14644207211044407>
88. Abdollahzadeh A, Bagheri B, Abassi M et al (2021) Comparison of the weldability of AA6061-T6 joint under different friction stir welding conditions. *J Mater Eng Perform* 30:1110–1127. <https://doi.org/10.1007/s11665-020-05379-4>
89. Petousis M, Vidakis N, Mountakis N et al (2023) On the substantial mechanical reinforcement of polylactic acid with titanium

- nitride ceramic nanofillers in material extrusion 3D printing. *Ceram Int* 49:16397–16411. <https://doi.org/10.1016/j.ceramint.2023.02.001>
90. Liaw CY, Tolbert JW, Chow LW, Guvendiren M (2021) Interlayer bonding strength of 3D printed PEEK specimens. *Soft Matter* 17:4775–4789. <https://doi.org/10.1039/d1sm00417d>
91. Shaffer S, Yang K, Vargas J et al (2014) On reducing anisotropy in 3D printed polymers via ionizing radiation. *Polymer (Guildf)* 55:5969–5979. <https://doi.org/10.1016/j.polymer.2014.07.054>
92. Chen J, Liu X, Tian Y et al (2022) 3D-printed anisotropic polymer materials for functional applications. *Adv Mater* 34:2102877. <https://doi.org/10.1002/adma.202102877>
93. Paspali A, Bao Y, Gawne DT et al (2018) The influence of nanostructure on the mechanical properties of 3D printed polylactide/nanoclay composites. *Compos Part B Eng* 152:160–168. <https://doi.org/10.1016/j.compositesb.2018.07.005>
94. Ambone T, Torris A, Shanmuganathan K (2020) Enhancing the mechanical properties of 3D printed polylactic acid using nanocellulose. *Polym Eng Sci* 60:1842–1855. <https://doi.org/10.1002/polb.25421>
95. Thomas WM, Threadgill PL, Nicholas ED (1999) Feasibility of friction stir welding steel. *Sci Technol Weld Join* 4:365–372. <https://doi.org/10.1179/136217199101538012>
96. Padmanaban R, Kishore VR, Balusamy V (2014) Numerical simulation of temperature distribution and material flow during friction stir welding of dissimilar aluminum alloys. *Procedia Eng* 97:854–863. <https://doi.org/10.1016/j.proeng.2014.12.360>
97. Nandan R, Roy GG, Lienert TJ, Debroy T (2007) Three-dimensional heat and material flow during friction stir welding of mild steel. *Acta Mater* 55:883–895. <https://doi.org/10.1016/j.actamat.2006.09.009>
98. Zhong YB, Wu CS, Padhy GK (2017) Effect of ultrasonic vibration on welding load, temperature and material flow in friction stir welding. *J Mater Process Technol* 239:273–283. <https://doi.org/10.1016/j.jmatprotec.2016.08.025>

Publisher's note Springer Nature remains neutral with regard to jurisdictional claims in published maps and institutional affiliations.